Intermittent supershear rupture punctuated by barrier-induced stopping phase during the 2025 $M_{\rm w}$ 7.8 Myanmar Earthquake: Evidence from near-fault strong motion observation

Xiaotian Ding¹, Shiqing Xu^{1,*}, Lingling Ye¹

¹Department of Earth and Space Sciences, Southern University of Science and Technology, Shenzhen, China

*Corresponding author: xusq3@sustech.edu.cn

Key points

- Supershear rupture occurred during the 2025 $M_{\rm w}$ 7.8 Myanmar earthquake but did not propagate under steady-state conditions
- A negative fault-parallel secondary pulse was recorded at a near-fault strong motion station NPW indicating rupture stopping phase
- A fault barrier at ~6 km south of the NPW station can explain the identified stopping phase as supported by numerical simulations

Abstract

Supershear rupture has been investigated by many studies, yet its exact characteristics during natural earthquakes are not fully clear, due to the paucity of near-field constraints. Here we analyze the strong motion data recorded at a near-fault station during the $2025\,M_{\rm w}\,7.8\,$ Myanmar earthquake to estimate the detailed source process around that station. By comparing simulated velocity waveforms under various conditions with the observed one, we find that a supershear rupture with speed surpassing $\sqrt{2}$ times S wave speed is required to fit the first-order features of the observation. Moreover, a fault barrier at $\sim 6\,$ km south of the station is inferred by the reversed-polarity fault-parallel secondary pulse following the main pulse, interpreted as a stopping phase. Together with other information, the results suggest an overall fast yet intermittent rupture process during the 2025 Myanmar earthquake, with the inferred barrier likely representing a segmentation boundary for the Sagaing fault.

Plain Language Summary

There is an active debate on whether supershear rupture propagates continuously or intermittently, raising the need to investigate the detailed process of supershear rupture and the related wavefield characteristics. The $2025 M_w 7.8$ Myanmar earthquake provides a good opportunity to probe this problem, due to the overall geometric simplicity of the central Sagaing fault that has long been proposed as a favorable condition for supershear rupture. In this study, we analyze the velocity waveform recorded at a near-fault station NPW to provide further insights into the source process of this earthquake. To do so, we conduct a series of computer simulations and compare the corresponding synthetic waveforms with the observed one. By optimizing waveform fit at the main pulse, we find that indeed a supershear rupture must be involved during the 2025 event. Moreover, a stopping phase indicative of fault barrier can be inferred by the reversed polarity of fault-parallel secondary pulse. These results support a local intermittent source process with supershear rupture interrupted by a barrier, which is otherwise difficult to resolve by far-field observations. Our study suggests that more near-field observations should be deployed to enhance the resolution and understanding of earthquake source process.

Keywords

supershear rupture, stopping phase, 2025 Myanmar earthquake, near-fault observation, fault segmentation

1. Introduction

Characterizing earthquake sources is important for understanding earthquake physics and assessing seismic hazards. One key source parameter is the rupture speed. Considerable effort has been made to clarify when rupture propagation can transition from below the S wave speed (subshear) to above (supershear) (Andrews, 1976; Wang et al., 2016; Bao et al., 2022), partly because supershear rupture can generate damaging S-wave Mach front over a long off-fault distance (Dunham & Archuleta, 2005; Bhat et al., 2007). Subsequent studies (Dunham, 2007; Cheng et al., 2023) also suggest a need to distinguish between sustained supershear under relatively homogeneous conditions (Bouchon & Vallée, 2003; Xia et al., 2004; Bouchon et al., 2010; Robinson et al., 2010; Liu et al., 2014) and intermittent (or transient, episodic) supershear

under heterogeneous conditions (Bruhat et al., 2016; Yao, 2017; Xu et al., 2023; Abdelmeguid et al., 2023; Delouis et al., 2024), thus it is important to test the related ideas using new observations.

Another important feature for studying earthquake sources is the reversed-polarity seismic phase produced by rupture arrest—called stopping phase (Savage, 1965; Page et al., 2005). Such phase is often accompanied by high-frequency radiation (especially under abrupt rupture arrest) (Madariaga, 1977, 1983), and it can be used to estimate source dimension and other parameters (Brüstle & Müller, 1987; Imanishi et al., 2004). Moreover, it is thought to be able to produce small-scale, reversed-polarity volumetric deformation within a large-scale fault stepover, implying the potential of inferring earthquake directivity from geomorphological features (Ben-Zion et al., 2012). Despite these various applications, a stopping phase was rarely captured by in-situ observations in the field, making it difficult to directly verify its related properties for natural earthquakes.

In this study, we show how supershear rupture and stopping phase can be jointly identified, based on the near-fault strong motion data recorded during the 2025 $M_{\rm w}$ 7.8 Myanmar earthquake. We further combine observed features with numerical simulations to infer a fault barrier within the overall rupture zone. The results demonstrate the high value of near-fault observations for constraining detailed source process.

2. The 2025 $M_{\rm w}$ 7.8 Myanmar earthquake

This earthquake occurred on March 28, 2025, along the central section of the 1400-km-long, right-lateral Sagaing fault that traverses Myanmar in the north-south direction (Fig. 1a). Several significant earthquakes with magnitude above 6.5 had occurred along or near the Sagaing fault since 1839 (Wang et al., 2014), but otherwise left a prominent seismic gap in the geometrically simple section in the center (Fig. 1a), which has been anticipated to host a damaging, potentially supershear earthquake in the future (Robinson et al., 2010; Hurukawa & Maung Maung, 2011; Xiong et al., 2017). The 2025 $M_{\rm w}$ 7.8 event (Ye et al., 2025) not only filled the identified seismic gap, but also penetrated into previously ruptured sections further to the north and south (Li et al., 2025; Fig. 1a).

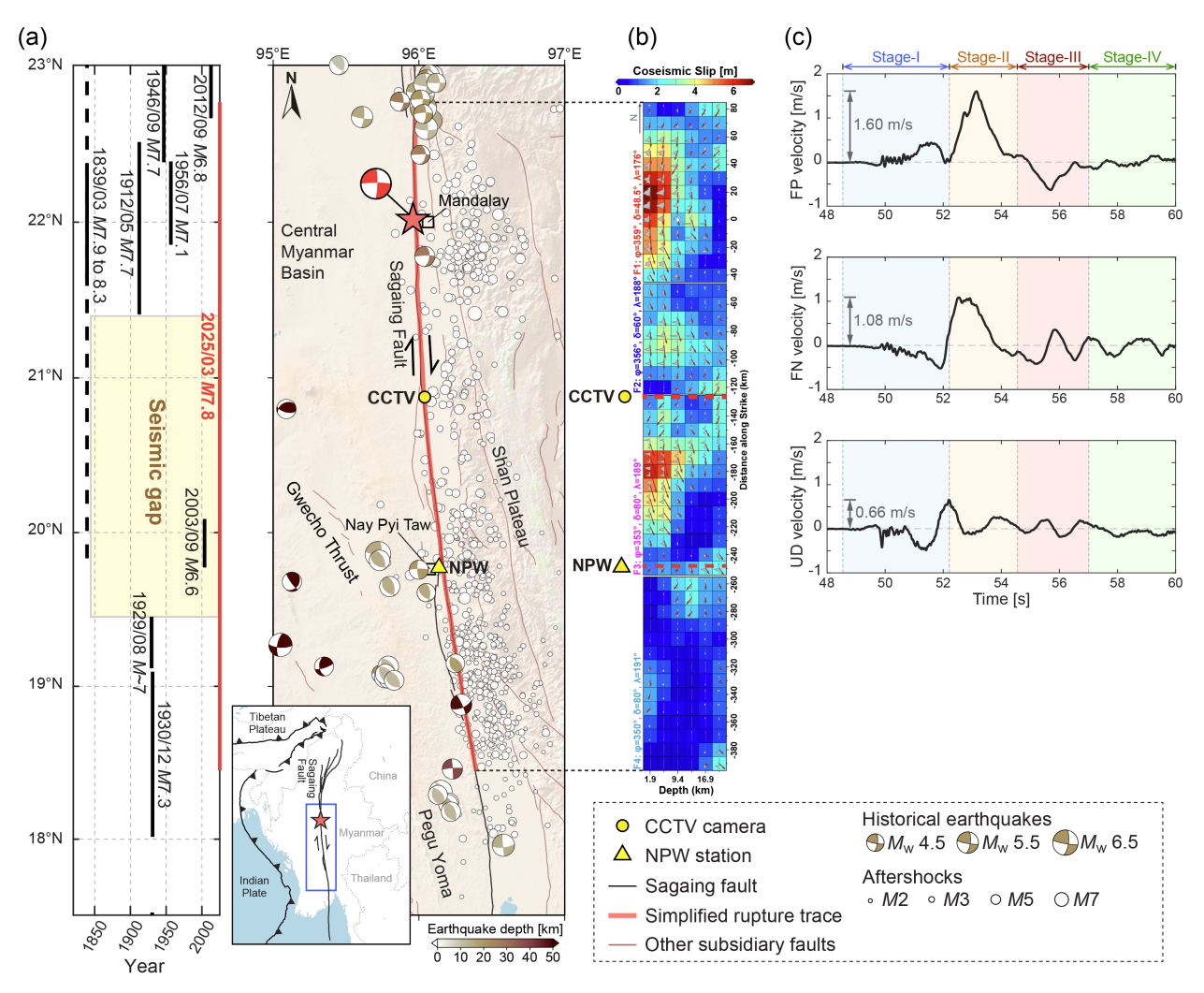


Figure 1. (a) Recent large earthquakes and tectonic setting for the studied area around the Sagaing fault in Myanmar. On the left, solid (dashed) black lines show the (inferred) extents of recent large earthquakes (Wang et al., 2014), with a seismic gap (yellow box) in the center until the occurrence of the 2025 $M_{\rm w}$ 7.8 earthquake (solid red line). On the right, black line and brown lines show the Sagaing fault and other subsidiary faults, respectively. The ruptured portion of the Sagaing fault during the 2025 earthquake is highlighted in red (modified after Benz et al. (2025)), with the red pentagram indicating the epicenter (Ye et al., 2025). Beachballs show the focal mechanisms for some historical earthquakes (1976/01/01–2025/03/27, with color indicating depth) and the 2025 mainshock (the red beachball, with $M_{\rm w}$ 7.7), based on the Global Centroid Moment Tensor (GCMT) catalog. Open circles show the aftershocks following the 2025 mainshock (2025/03/28-2025/04/28), based on the Thai Meteorological Department (TMD) catalog. Yellow circle and triangle indicate the location of a CCTV camera and strong motion station (NPW) near the Sagaing fault, respectively. (b) Coseismic source model over four subfaults (F1–F4) for the 2025 Myanmar earthquake, taken from Ye et al. (2025). Color shows the magnitude of slip on each subfault patch, with vectors indicating slip direction (eastern side relative to western side) and slip amount (implied by vector length) and gray polygons indicating the corresponding source time function. (c) Three-component, velocity waveform recorded at the NPW station (see text for more details).

Several research groups have estimated the source process of the 2025 event, revealing the following first-order picture (Inoue et al., 2025; Ye et al., 2025). The earthquake started near the city Mandalay, and then expanded energetically over ~50 km in both north and south directions. After about 40 s, it turned into a unilateral rupture primarily propagating to the south and continued for another 50 s. The final rupture had a total length of 460-480 km (Fig. 1b), representing one of the longest strike-slip earthquakes, possibly aided by rupture along a bimaterial interface (Shi & Ben-Zion, 2006) and a narrowed rupture zone with gradually tapered slip toward the south (Li et al., 2025; USGS, 2025).

Regarding the details, while some studies imply a relatively smooth source process including a sustained supershear toward the south (Vera et al., 2025; Li et al., 2025), others suggest otherwise. For instance, the inverted results based on teleseismic data (e.g., Inoue et al., 2025; Ye et al., 2025) show a rather patchy slip distribution, with high slip concentrated around the hypocenter and ~180 km to the south (Fig. 1b). Analyses of data recorded at a near-fault CCTV (Closed Circuit Television) camera and strong motion station NPW (see locations in Fig. 1) also favor an intermittent source process with episodic rupture deceleration and acceleration (Hirano et al., 2025). Below we analyze the data recorded at the NPW station (near the city Nay Pyi Taw) to further support the view of intermittent source process, by highlighting a supershear transient punctuated by barrier-induced stopping phase.

3. Data and Methods

3.1. Strong motion data at the NPW station

The raw strong motion data recorded at the NPW station, corresponding to the unprocessed acceleration, were downloaded from the IRIS data center. We removed the instrument response and applied baseline correction using the method proposed by Wang et al. (2011). We did not make correction for the clock drift, since the accumulative time error was less than 1 s (Lai et al., 2025), which would not significantly affect the subsequent waveform analysis. Then we integrated the processed acceleration over time to obtain velocity, and rotated the results into fault-parallel (FP), fault-normal (FN) and up-down (UD) components based on the local fault geometry (Figs. 1a and 1c), with positive indicating N7°W, N83°E and up, respectively.

For convenience, we divide the velocity waveform into four stages (Fig. 1c): early part (Stage-II), main pulse (Stage-II), secondary pulse (Stage-III), and trailing part (Stage-IV). Starting with the main pulse (Stage-II), a simple comparison between the FP and FN components yields an amplitude ratio of $\Delta \dot{u}_{FP}^s / \Delta \dot{u}_{FN}^s = \sqrt{V_r^2/C_s^2-1} > 1$ (Mello et al., 2016), indicating a local rupture speed V_r above $\sqrt{2}C_S$ (C_S being S wave speed). This estimation is consistent with the detailed waveform pattern at the FP main pulse (Stage-II), where the S-wave Mach front appears as a local peak (rather than a local trough) following the initial peak of the P-wave dilatational field (fig. 2d in Dunham & Archuleta (2005)). It is also interesting to note that the UD component generally shows an opposite polarity to the FP component during Stage-I, and the FP secondary pulse (Stage-III) shows an opposite polarity to the FP main pulse (Stage-II) (Fig. 1c). While the former may reflect the Poisson effect related to head and direct waves (Section 5), the latter is less intuitive to understand and will be investigated by numerical simulations.

3.2. Setup of numerical simulations

To provide additional insights into the source process near the NPW station, we conduct numerical simulations of dynamic ruptures. The setup of numerical simulations is based on the kinematic source model of Ye et al. (2025), which shows a cascading rupture process over four subfaults (Fig. 1b). Previous studies suggest that each episode in a cascading rupture process may be considered as a subevent, with renewed initial state taking into account the stress transfer from the earlier episode(s) (Xu et al., 2023; Ding et al., 2023). Therefore, here we do not model the 2025 Myanmar earthquake from the very beginning, but rather focus on the rupture process on subfault F3 (Fig. 1b), with a particular interest in comparing simulated synthetic waveform with the observed one at the NPW station.

We simulate both 2.5D and 3D dynamic ruptures along a vertical, ~7.5 km-wide strike-slip subfault (after mapping to half space), following and simplifying the inverted results for F3 (Fig. 1b). The 2.5D simulations are used to explore the waveform fit in the FP and FN components over a large parameter space, while the 3D simulations are used to check the additional fit in the UD component. Time-weakening and slip-weakening friction laws are respectively employed to control the rupture evolution within and beyond the nucleation stage, as in Ding et al. (2023). We test a variety of

rupture modes and speeds approaching the target NPW station, by tuning rupture nucleation and other conditions on the modeled subfault. Given the inverted result that the NPW station resides close to a local slip minimum (Fig. 1b), we sometimes include a fault barrier in numerical simulations to investigate its impact on the synthetic waveform. More details about numerical simulations are given in the Supporting Information (Text S1–S9, Figs. S1–S5, Tables S1 and S2).

4. Results

4.1. Reference cases without a fault barrier

We first examine the reference cases without a fault barrier. Figure 2 presents the simulated velocity field under the 2.5D model and the related waveform fit for two supershear ruptures with $V_{\rm r}>\sqrt{2}{\it C}_{\rm S}$ (${\it C}_{\rm S}=3310\,{\rm m/s}$, Text S2). As can be seen, both cases, though somewhat underestimating the FN main pulse, provide an overall good fit to the FP main pulse, including the general amplitude and the appearance of two local peaks (Stage-II in Figs. 2b and 2d). Our additional tests show that a subshear rupture or an incipient supershear rupture that has just transitioned from subshear tends to produce a larger FN main pulse than the FP counterpart, inconsistent with the observation (Figs. S6 and S7). Moreover, a (quasi)steady-state supershear rupture with $V_r \lesssim \sqrt{2}C_S$ tends to produce an S-wave trough behind the initial P-wave peak in the FP component or out-of-phase FP and FN main pulses, also inconsistent with the observation (Fig. S8). Returning to Fig. 2, the first case (Figs. 2a and 2b), simulated under a mother-daughter transition (MDT), shows a stronger trailing Rayleigh phase than the second case (Figs. 2c and 2d) under a direct transition (DT) (see Bizzarri & Liu (2016) and Xu et al. (2023) for more information about MDT and DT). In particular, the first case under MDT produces a much larger trailing pulse than the main pulse in the FN component, incompatible with the observed trend (Fig. 2b). Based on all the above, we conclude that a well-developed supershear transient, likely with $V_r > \sqrt{2}C_S$ but without strong trailing Rayleigh phase(s), is required to fit the first-order features of the observation at the NPW station. We also note that the supershear case under DT (Fig. 2c), though satisfying the above requirement, still cannot fit the observed negative FP pulse during Stage-III (Fig. 2d), which calls for the need to incorporate other model ingredients.

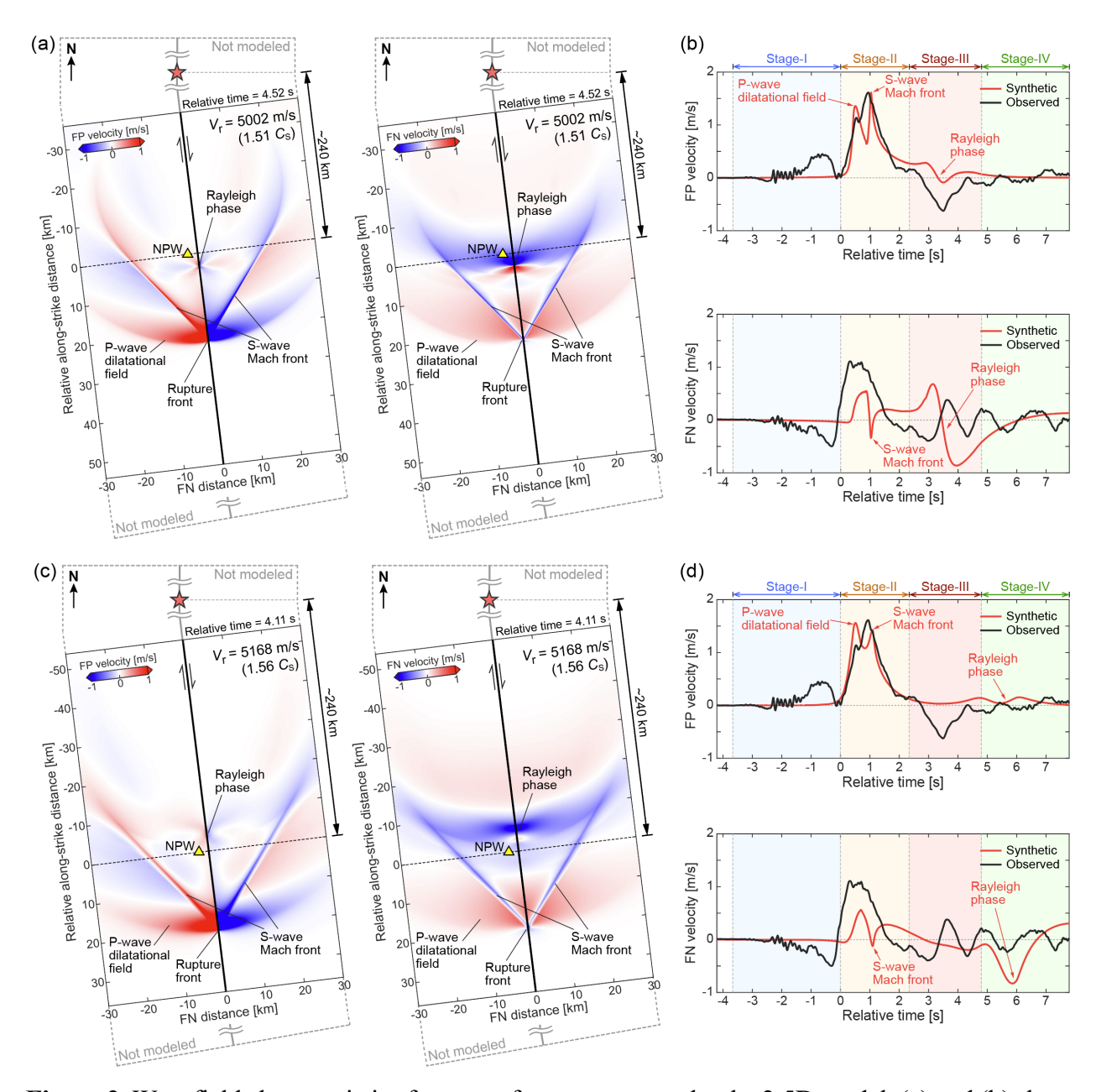


Figure 2. Wavefield characteristics for two reference cases under the 2.5D model. (a) and (b) show the simulated velocity wavefield for a supershear rupture under a mother-daughter transition (MDT) and the related waveform fit with data at the NPW station. (c) and (d) show similar results as in (a) and (b) but for a supershear rupture under a direct transition (DT). In (a) and (c), relative alongstrike distance zero is aligned to the NPW station, which itself is ~240 km south of the epicenter (red pentagram) and ~2.5 km west of the fault (Lai et al., 2025). In (b) and (d), relative time zero is aligned to the onset of observed FP pulse (in black) during Stage-II.

4.2. Preferred cases with a fault barrier

Inspired by the known properties of stopping phase (Section 1) and the close proximity of NPW station to a local slip minimum (Section 3.2), we further incorporate a fault barrier into the supershear cases under DT, in order to test if the added barrier can cause a reversed-polarity secondary pulse in the FP component. Simulated results under the 2.5D model show that indeed the barrier, here modeled as a patch with spatially decreased initial shear stress, can produce a negative secondary pulse (Stage-III) in the FP component (Fig. 3b). By comparing more near-fault synthetic waveforms with the evolution of on-fault slip velocity, we find that the negative pulse observed at the NPW station is associated to the northward-propagating part of a stopping phase (Figs. 3a and S9). While such phase can cause a negative FP velocity off the fault, in the performed simulations it only permits a temporary relocking (zero instead of negative slip velocity) exactly on the fault due to frictional constraint (Fig. S9). We further conduct a detailed parameter-space study, by exploring waveform fit against data during Stage-I to III (Text S8) under various conditions of (negative) stress gradient, barrier location and slip-weakening distance (Fig. 3c). The results suggest that in the preferred case(s) the barrier should be located at ~6 km south of the NPW station, and the absolute value of stress gradient must be relatively high (Fig. 3d), otherwise the relative timing or the amplitude of the negative FP pulse cannot be reproduced (Figs. S10– S12). We also make another set of tests by replacing decreased initial shear stress with increased normal stress or static friction coefficient, and obtain similar conclusions (Figs. S13 and S14). By transforming the preferred case(s) from 2.5D to 3D under a comparable model setup (Text S1), we find that the transformed case(s) can also provide a good fit to the UD component, at least during Stage-II and/or III (Figs. S15–S17).

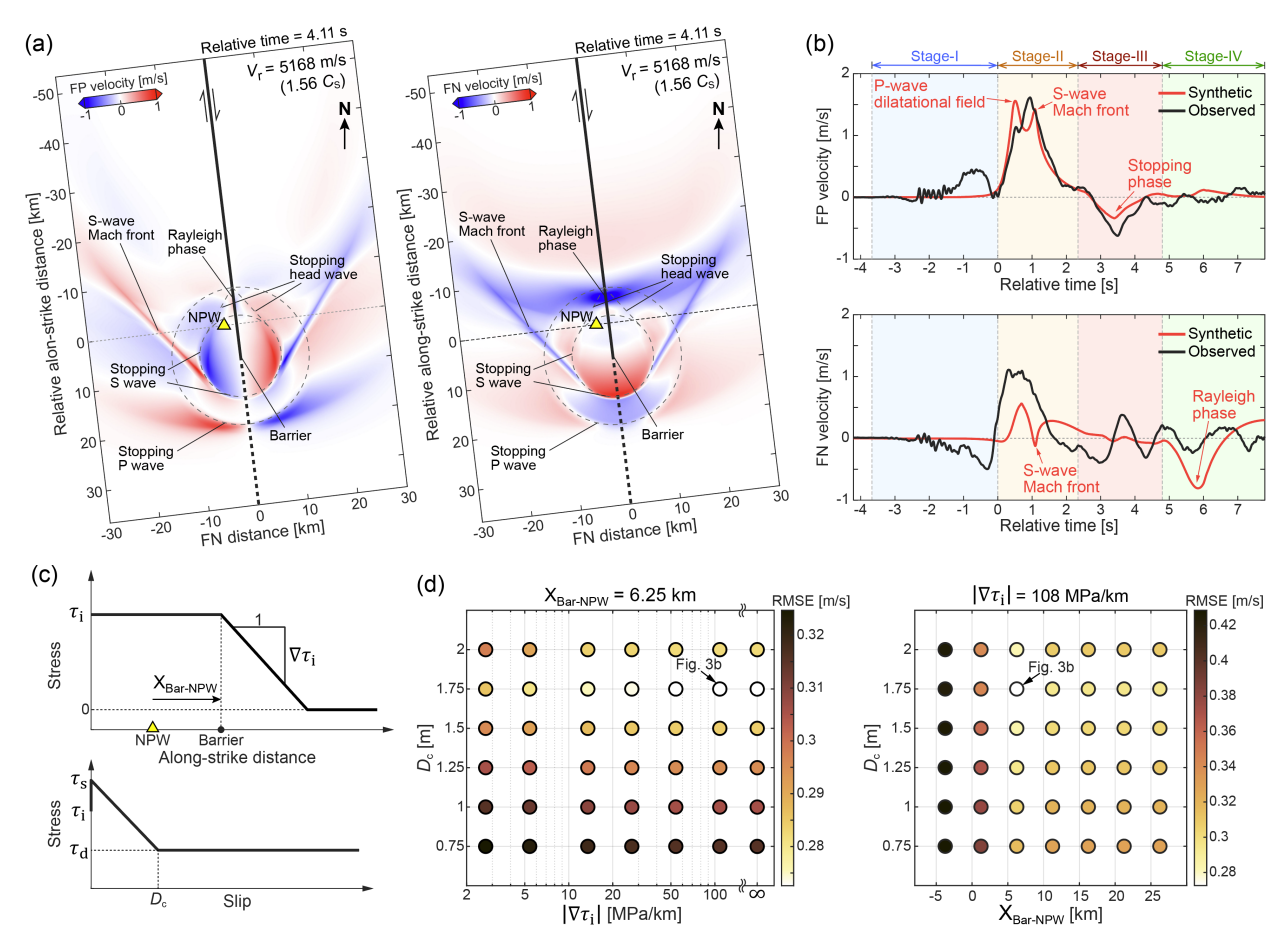


Figure 3. Wavefield characteristics for a preferred case under the 2.5D model and the related phase diagrams for constraining the properties of an added barrier. (a) and (b) show the simulated velocity wavefield for a barrier-impeded supershear rupture under DT and the related waveform fit with data at the NPW station. In (a), major wavefronts of the stopping phase are marked by dashed lines. (c) Definitions of decreasing gradient of initial shear stress $(\nabla \tau_i)$, location of barrier relative to NPW station $(X_{Bar-NPW})$ and slip-weakening distance (D_c) , with τ_s and τ_d indicating static and dynamic strength, respectively (Text S3). (d) Phase diagrams summarizing waveform fit in terms of root-mean-square-error (RMSE, see Text S8) over a range of D_c , $|\nabla \tau_i|$ and $X_{Bar-NPW}$.

5. Discussion and conclusions

We have analyzed the near-fault strong motion data recorded at the NPW station. By integrating the observed waveform characteristics, simulation results and other available information, we now provide an in-depth discussion on the source process of the 2025 $M_{\rm w}$ 7.8 Myanmar earthquake. At the macroscopic scale, the southward rupture did not propagate smoothly with an average supershear speed of 4615 m/s ($\lesssim \sqrt{2}C_{\rm s}$) (according to the epicentral distance of ~240 km and the

arrival time of ~52 s at the NPW station), but had episodic acceleration and deceleration, possibly involving supershear around the hypocenter, subshear around the CCTV camera and supershear again (likely with $V_r > \sqrt{2}C_s$) around the NPW station (Inoue et al., 2025; Hirano et al., 2025; Figs. 1 and 3). This large-scale intermittent process is also supported by the coseismic slip distribution, with one low slip patch lying between two high ones (Inoue et al., 2025; Ye et al., 2025; Fig. 4), corresponding to the estimated subshear and supershear episode(s), respectively (Hirano et al., 2025). Similar rupture behaviors, characterized by supershear-subshear-supershear transition and undulant slip distribution, have been repeatedly observed on a laboratory fault with stress heterogeneities (Xu et al., 2023), suggesting that the 2025 Myanmar earthquake may also be modulated by stress heterogeneities.

At the local scale, the rupture evolution on subfault F3 showed multiple slip pulses associated with strong spatial heterogeneity (Fig. 1b) and was impacted by an inferred barrier near the NPW station (Figs. 3 and 4), also contributing to an intermittent process. More evidences for the inferred barrier can involve the following features near the NPW station: (a) high-frequency source radiators (Li et al., 2025) including some back-propagating ones (Vera et al., 2025), (b) clustered aftershocks in contrast with fewer ones to the north (Peng et al., 2025; Fig. 4), (c) coincidence with the southern end of the previously identified seismic gap (Li et al., 2025; Fig. 4), (d) relatively low slip and/or low stress drop reported by other studies (Li et al., 2025; USGS, 2025), (e) structural complexities such as fault discontinuity, branching and bend (fig. 19.9c in Tun & Watkinson (2017); Fig. 4), and (f) localized reverse-type faulting and seismicity (fig. 19.2 in Tun & Watkinson (2017); Fig. 4) indicating a local high angle of maximum compressive stress to the Sagaing fault (see Mount & Suppe (1987) and Miller (1998) for a corresponding discussion on the San Andreas fault). Therefore, although we cannot rule out other possibilities for interpreting the negative FP secondary pulse recorded at the NPW station, such as the negative loading from fault-zonereflected waves (Huang & Ampuero, 2011), we think barrier-induced stopping phase should stand out as a strongly-supported explanation (Figs. 3, 4, S15–S17). While we have further constrained the starting position and strength of the inferred barrier (Figs. 3, S13 and S14), it is difficult to estimate its ending position on the other side by current simulations. Nonetheless, we expect the barrier to exhibit a moderate size at most (Fig. 4), since the actual rupture could continue its propagation further to the south (Ye et al., 2025; USGS, 2025).

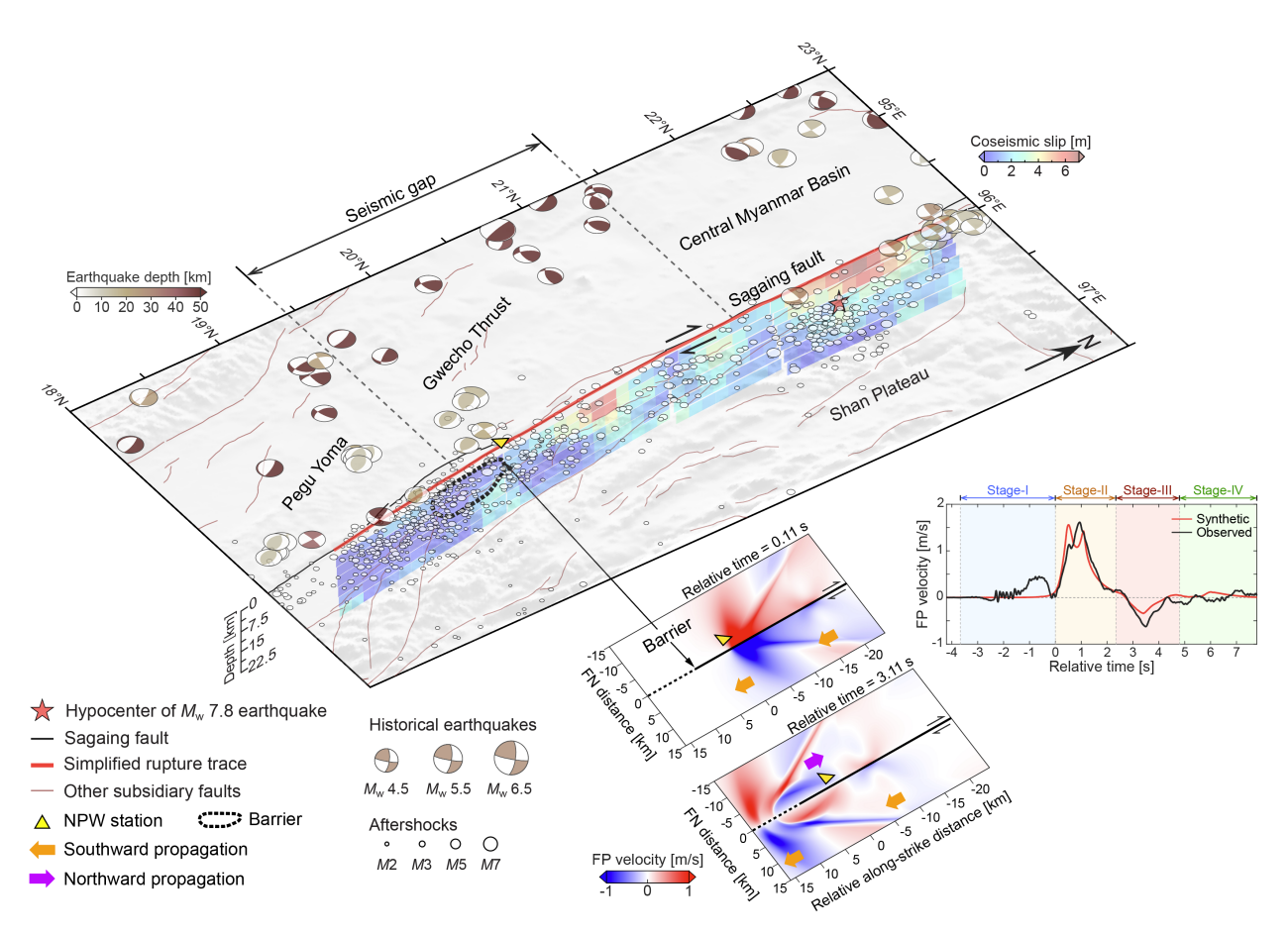


Figure 4. Perspective view of seismological and geological features around the 2025 $M_{\rm w}$ 7.8 Myanmar earthquake rupture zone. Color-coded beachballs show the focal mechanisms and depth information for some historical earthquakes according to the GCMT catalog, and open circles show the distribution of aftershocks (projected onto ground surface) according to the TMD catalog (see Fig. 1 for more information). Color-coded patches show the coseismic slip distribution determined by Ye et al. (2025), with the red pentagram indicating the mainshock hypocenter. Plots at the bottom right show the simulated FP velocity under the preferred case and the corresponding waveform fit with data. The position and possible spatial extent of the inferred barrier are depicted by the dashed black line to the south of the NPW station.

Taken together, the discussed intermittent source process supports the view of fault segmentation as one of the criteria for distinguishing some large earthquakes from small ones (Lay & Kanamori, 1981; Aki, 1984; Manighetti et al., 2007; Xu et al., 2018; Klinger, 2022; Cui et al., 2025). Specifically, the inferred barrier near the NPW station (Fig. 4) likely represents a segmentation boundary for the Sagaing fault. On one hand, it may serve as an external barrier to fully stop some small earthquakes around 19.5°N (Fig. 1), with their sources described by a compact, simply-

connected region (Manighetti et al., 2007) with near-constant rupture speed (Kaneko & Shearer, 2015). Under such condition, observable high-frequency radiation to the far field mainly reflects the starting and/or stopping of the overall rupture process (Madariaga, 1977; Imanishi et al., 2004; Li et al., 2022). On the other hand, it can behave as an internal barrier (e.g., partially-ruptured or bypassed patch) within the overall source region of an elongated large earthquake, with ability to cause additional high-frequency radiation, internal stress drop deficit or even stress concentration, and multiple peaks in moment rate function (Madariaga, 1979), as supported by the observational results for the 2025 M_w 7.8 event (Ye et al., 2025; Li et al., 2025; Vera et al., 2025).

It is worth noting that some of the observed waveform features still cannot be fitted by the preferred synthetics (Figs. 3), including (a) earlier signals carrying some high-frequency content during Stage-I, (b) the descending slope without a subsequent ascending one at the FN main pulse during Stage-II, and (c) the enduring oscillations during Stage-III and IV. This suggests that more complexities may be involved in the 2025 Myanmar earthquake but are not modeled by current simulations. Nonetheless, we can propose tentative ideas for understanding these features, assuming that they reflect true source, path or site effects rather than instrumental errors. Due to the earlier arrival, feature-(a) may represent head wave refracted from the Moho or the bimaterial Sagaing fault (e.g., Ben-Zion, 1990) and/or direct wave radiated by earlier-stage rupture (Peng et al., 2025), with the high-frequency content indicating P-wave-triggered failure or nonlinear response in the shallow subsurface (Sleep, 2018; Sleep & Ma, 2008) and/or local damage-related radiation (Ben-Zion et al., 2024). Feature-(b) is rather intriguing at first glance, as it would contrast with the predicted opposite polarities for FP and FN components at the Mach front (Figs. 2 and S8), where pure shear deformation (zero divergence) is expected to dominate (Mello et al., 2016). Possible ways for reconciling this conflict and the mismatch in FN pulse amplitude could be to incorporate a depth-varying source process (Fig. 1b) and/or material heterogeneity (Xu & Ben-Zion, 2017; Abdelmeguid et al., 2025). Finally, feature-(c) may stem from various trapping effects of a sedimentary basin (Somerville & Graves, 2003) or low-velocity fault zone (Huang & Ampuero, 2011; Xu et al., 2015), especially considering that the NPW station resides in the southwestern (extensional) quadrant of the 2025 Myanmar earthquake, where the central Myanmar basin (Tun & Watkinson, 2017) and off-fault rock damage can indeed play a role. Future work can be done to test the above ideas via more sophisticated 3D numerical simulations.

In summary, our study by identifying supershear rupture and stopping phase at a near-fault strong motion station has provided valuable insights into the 2025 $M_{\rm w}$ 7.8 Myanmar earthquake, such as an intermittent source process and the existence of a fault barrier. The results once again demonstrate the significance and value of near-fault observations (Ben-Zion, 2019). Previously near-fault observations have been employed to estimate fracture energy and/or slip-weakening distance of dynamic ruptures (Fukuyama & Mikumo, 2007; Cruz-Atienza & Olsen, 2010; Svetlizky et al., 2019; Xu et al., 2019), to characterize various rupture modes including supershear rupture under different generation conditions (Dunham & Archuleta, 2004; Bizzarri & Liu, 2016; Xu et al., 2023), to clarify rupture and wave phases (Yao & Yang, 2025), and to recognize high-order re-rupture behind a primary rupture (Ding et al., 2024). With more deployments of near-fault observations, more properties previously proposed for earthquake sources can be tested, while some unexpected, new results may be discovered as well.

Acknowledgments

This study was supported by the National Natural Science Foundation of China (42474082) and the Guangdong Program (2021QN02G106).

Open Research

Data Availability Statement

The software SEM2DPACK for conducting 2.5D simulations is available https://github.com/jpampuero/sem2dpack (Ampuero, 2012). The software SPECFEM3D for conducting 3D simulations is available at https://doi.org/10.5281/zenodo.10823181 (Komatitsch et al., 2024). The input parameters for performing numerical simulations are within the paper. The database for geological faults in Myanmar is available at https://doi.org/10.13140/RG.2.2.25509.58084 (Bachmanov et al., 2022). The surface rupture trace data for the 2025 Myanmar earthquake can be found from Benz et al. (2025). Information of earthquake focal mechanisms can be found from the Global Centroid Moment Tensor (GCMT) 2012). Information of aftershocks be found project (Ekström et al., can https://www.fdsn.org/networks/detail/TM/ (Thai Meteorological Department, 2008). The raw strong motion data can be downloaded from the Incorporated Research Institutions for Seismology

(IRIS) data management center at https://ds.iris.edu/wilber3/find_stations/11952284. Some of the figures were drawn by the Generic Mapping Tools (GMT) (Wessel et al., 2019).

References

Abdelmeguid, M., Zhao, C., Yalcinkaya, E., Gazetas, G., Elbanna, A., & Rosakis, A. (2023). Dynamics of episodic supershear in the 2023 M7. 8 Kahramanmaraş/Pazarcik earthquake, revealed by near-field records and computational modeling. *Communications Earth & Environment*, 4, 456. https://doi.org/10.1038/s43247-023-01131-7

Abdelmeguid, M., Elbanna, A., & Rosakis, A. (2025). Ground motion characteristics of subshear and supershear ruptures in the presence of sediment layers. *Geophysical Journal International*, 240(2), 967–987. https://doi.org/10.1093/gji/ggae422

Aki, K. (1984). Asperities, barriers, characteristic earthquakes and strong motion prediction. Journal of Geophysical Research: Solid Earth, 89(B7), 5867–5872. https://doi.org/10.1029/JB089iB07p05867

Ampuero, J.-P. (2012). SEM2DPACK—A spectral element method tool for 2D wave propagation and earthquake source dynamics [Software]. https://github.com/jpampuero/sem2dpack

Andrews, D. J. (1976). Rupture velocity of plane strain shear cracks. *Journal of Geophysical Research*, 81(32), 5679–5687. https://doi.org/10.1029/JB081i032p05679

Bachmanov, D. M., Trifonov, V. G., Kozhurin, A. I., & Zelenin, E. A. (2022). Active Faults of Eurasia Database AFEAD v2022 [Dataset]. *ResearchGate*. https://doi.org/10.13140/RG.2.2.25509.58084

Bao, H., Xu, L., Meng, L., Ampuero, J.-P., Gao, L., & Zhang, H. (2022). Global frequency of oceanic and continental supershear earthquakes. *Nature Geoscience*, 15, 942–949. https://doi.org/10.1038/s41561-022-01055-5

Ben-Zion, Y. (1990). The response of two half spaces to point dislocations at the material interface. *Geophysical Journal International*, 101(3), 507–528. https://doi.org/10.1111/j.1365-246X.1990.tb05567.x

Ben-Zion, Y., Rockwell, T. K., Shi, Z., & Xu, S. (2012). Reversed-polarity secondary deformation structures near fault stepovers. *Journal of Applied Mechanics*, 79(3), 031025. https://doi.org/10.1115/1.4006154

Ben-Zion, Y. (2019). A critical data gap in earthquake physics. *Seismological Research Letters*, 90(5), 1721–1722. https://doi.org/10.1785/0220190167

Ben-Zion, Y., Zhang, S., & Meng, X. (2024). Isotropic high-frequency radiation in near-fault seismic data. *Geophysical Research Letters*, 51(17), e2024GL110303. https://doi.org/10.1029/2024GL110303

- Benz, H., Furlong, K., Herman, M., McKenzie, K., Schmitt, R., Reitman, N., Thompson, E., Barnhart, W., Yeck, W., & Pananont, P. (2025). 2025 M 7.7 Mandalay, Burma (Myanmar) Earthquake [Dataset]. *U.S. Geological Survey StoryMap*, https://storymaps.arcgis.com/stories/5f3e33e35c5247c9bf5204fa0d6e56e5
- Bhat, H. S., Dmowska, R., King, G. C. P., Klinger, Y., & Rice, J. R. (2007). Off-fault damage patterns due to supershear ruptures with application to the 2001 $M_{\rm w}$ 8.1 Kokoxili (Kunlun) Tibet earthquake. *Journal of Geophysical Research*, 112(B6), B06301. https://doi.org/10.1029/2006JB004425
- Bizzarri, A., & Liu, C. (2016). Near-field radiated wave field may help to understand the style of the supershear transition of dynamic ruptures. *Physics of the Earth and Planetary Interiors*, 261, 133–140. https://doi.org/10.1016/j.pepi.2016.05.013
- Bouchon, M., & Vallée, M. (2003). Observation of long supershear rupture during the magnitude 8.1 Kunlunshan earthquake. *Science*, 301(5634), 824–826. https://doi.org/10.1126/science.1086832
- Bouchon, M., Karabulut, H., Bouin, M.-P., Schmittbuhl, J., Vallée, M., Archuleta, R., Das, S., Renard, F., & Marsan, D. (2010). Faulting characteristics of supershear earthquakes. *Tectonophysics*, 493(3–4), 244–253. https://doi.org/10.1016/j.tecto.2010.06.011
- Brüstle, W., & Müller, G. (1987). Stopping phases in seismograms and the spatiotemporal extent of earthquakes. *Bulletin of the Seismological Society of America*, 77(1), 47–68. https://doi.org/10.1785/BSSA0770010047
- Bruhat, L., Fang, Z., & Dunham, E. M. (2016). Rupture complexity and the supershear transition on rough faults. *Journal of Geophysical Research: Solid Earth*, 121(1), 210–224. https://doi.org/10.1002/2015JB012512
- Cheng, C., Wang, D., Yao, Q., Fang, L., Xu, S., Huang, Z., Liu, T., Wang, Z., & Huang, X. (2023). The 2021 Mw 7.3 Madoi, China earthquake: Transient supershear ruptures on a presumed immature strike-slip fault. *Journal of Geophysical Research: Solid Earth*, 128(2), e2022JB024641. https://doi.org/10.1029/2022JB024641
- Cruz-Atienza, V. M., & Olsen, K. B. (2010). Supershear Mach-waves expose the fault breakdown slip. *Tectonophysics*, 493(3–4), 285–296. https://doi.org/10.1016/j.tecto.2010.05.012
- Cui, Y., Li, S., Chen, L., & Aoki, Y. (2025). Large megathrust earthquakes tend to sustain an increasingly longer duration than expected. *Geophysical Research Letters*, 52(8), e2024GL112985. https://doi.org/10.1029/2024GL112985
- Delouis, B., van den Ende, M., & Ampuero, J.-P. (2024). Kinematic rupture model of the 6 February 2023 $M_{\rm w}$ 7.8 Türkiye Earthquake from a large set of near-source strong-motion records

combined with GNSS offsets reveals intermittent supershear rupture. *Bulletin of the Seismological Society of America*, 114(2), 726–740. https://doi.org/10.1785/0120230077

Ding, X., Xu, S., Xie, Y., van den Ende, M., Premus, J., & Ampuero, J.-P. (2023). The sharp turn: Backward rupture branching during the 2023 $M_{\rm w}$ 7.8 Kahramanmaraş (Türkiye) earthquake. *Seismica*, 2(3). https://doi.org/10.26443/seismica.v2i3.1083

Ding, X., Xu, S., Fukuyama, E., & Yamashita, F. (2024). Back-propagating rupture: Nature, excitation, and implications. *Journal of Geophysical Research: Solid Earth*, 129(10), e2024JB029629. https://doi.org/10.1029/2024JB029629

Dunham, E. M., & Archuleta, R. J. (2004). Evidence for a supershear transient during the 2002 Denali fault earthquake. *Bulletin of the Seismological Society of America*, 94(6B), S256–S268. https://doi.org/10.1785/0120040616

Dunham, E. M., & Archuleta, R. J. (2005). Near-source ground motion from steady state dynamic rupture pulses. *Geophysical Research Letters*, 32(3), L03302. https://doi.org/10.1029/2004GL021793

Dunham, E. M. (2007). Conditions governing the occurrence of supershear ruptures under slip-weakening friction. *Journal of Geophysical Research*, 112(B7), B07302. https://doi.org/10.1029/2006JB004717

Ekström, G., Nettles, M., & Dziewoński, A. M. (2012). The global CMT project 2004–2010: Centroid-moment tensors for 13,017 earthquakes. *Physics of the Earth and Planetary Interiors*, 200, 1–9. https://doi.org/10.1016/j.pepi.2012.04.002

Fukuyama, E., & Mikumo, T. (2007). Slip-weakening distance estimated at near-fault stations. *Geophysical Research Letters*, 34(9), L09302. https://doi.org/10.1029/2006GL029203

Hirano, S., Doke, R., & Maeda, T. (2025). Supershear-subshear-supershear rupture associated with the 2025 Mandalay Earthquake in Myanmar. *Seismica*, 4(2). https://doi.org/10.26443/seismica.v4i2.1785

Huang, Y., & Ampuero, J.-P. (2011). Pulse-like ruptures induced by low-velocity fault zones. *Journal of Geophysical Research*, 116(B12), B12307. https://doi.org/10.1029/2011JB008684

Hurukawa, N., & Maung Maung, P. (2011). Two seismic gaps on the Sagaing Fault, Myanmar, derived from relocation of historical earthquakes since 1918. *Geophysical Research Letters*, 38(1), L01310. https://doi.org/10.1029/2010GL046099

Imanishi, K., Takeo, M., Ellsworth, W. L., Ito, H., Matsuzawa, T., Kuwahara, Y., Iio, Y., Horiuchi, S., & Ohmi, S. (2004). Source parameters and rupture velocities of microearthquakes in Western Nagano, Japan, determined using stopping phases. *Bulletin of the Seismological Society of America*, 94(5), 1762–1780. https://doi.org/10.1785/012003085

- Inoue, N., Yamaguchi, R., Yagi, Y., Okuwaki, R., Enescu, B., & Tadapansawut, T. (2025). A multiple asymmetric bilateral rupture sequence derived from the peculiar tele-seismic P-waves of the 2025 Mandalay, Myanmar earthquake. *Seismica*, *4*(1). https://doi.org/10.26443/seismica.v4i1.1691
- Kaneko, Y., & Shearer, P. M. (2015). Variability of seismic source spectra, estimated stress drop, and radiated energy, derived from cohesive-zone models of symmetrical and asymmetrical circular and elliptical ruptures. *Journal of Geophysical Research: Solid Earth*, 120(2), 1053–1079. https://doi.org/10.1002/2014JB011642
- Klinger, Y. (2022). Imprint of the continental strike-slip fault geometrical structure in geophysical data. *Geophysical Research Letters*, 49(11), e2022GL098146. https://doi.org/10.1029/2022GL098146
- Komatitsch, D., Tromp, J., Garg, R., Gharti, H. N., Nagaso, M., Oral, E., Peter, D., Afanasiev, M., Almada, R., Ampuero, J.-P., Bachmann, E., Bai, K., Basini, P., Beller, S., Bishop, J., Bissey, F., Blitz, C., Bottero, A., Bozdag, E., Casarotti, E., Charles, J., Chen, M., Cristini, P., Durochat, C., Galvez Barron, P., Gassmoeller, R., Goeddeke, D., Grinberg, L., Gupta, A., Heien, E., Hjoerleifsdottir, V., Karakostas, F., Kientz, S., Labarta, J., Le Goff, N., Le Loher, P., Lefebvre, M., Liu, Q., Liu, Y., Luet, D., Luo, Y., Maggi, A., Magnoni, F., Martin, R., Matzen, R., McBain, G. D., McRitchie, D., Meschede, M., Messmer, P., Michea, D., Miller, D., Modrak, R., Monteiller, V., Morency, C., Nadh Somala, S., Nissen-Meyer, T., Pouget, K., Rietmann, M., Sales de Andrade, E., Savage, B., Schuberth, B., Sieminski, A., Smith, J., Strand, L., Tape, C., Valero Cano, E., Videau, B., Vilotte, J.-P., Weng, H., Xie, Z., Zhang, C., & Zhu, H. (2024). SPECFEM/specfem3d: SPECFEM3D v4.1.1 [Software]. *Zenodo*. https://doi.org/10.5281/zenodo.10823181
- Lay, T., & Kanamori, H. (1981). An asperity model of large earthquake sequences. In Simpson, D. W., & Richards, P. G. (Eds.), *Earthquake prediction: An international review, Maurice Ewing Series* (Vol. 4, pp. 579–592). Washington, DC: American Geophysical Union. https://doi.org/10.1029/ME004p0579
- Lai, S.-T., Oo, K. M., Htwe, Y. M. M., Yi, T., Than, H. H., Than, O., Min, Z., Oo, T. M., Maung, P. M., Bindi, D., Cotton, F., Evans, P. L., Heinloo, A., Hillmann, L., Saul, J., Sens-Schoenfelder, C., Strollo, A., Tilmann, F., Weatherill, G., Yen, M.-H., Zaccarelli, R., Zieke, T., & Milkereit, C. (2025). Capacity building enables unique near-fault observations of the destructive 2025 M_w 7.7 Myanmar Earthquake. *Earth System Science Data Discussion [Preprint]*. https://doi.org/10.5194/essd-2025-216
- Li, B., Wu, B., Bao, H., Oglesby, D. D., Ghosh, A., Gabriel, A.-A., Meng, L., & Chu, R. (2022). Rupture heterogeneity and directivity effects in back-projection analysis. *Journal of Geophysical Research: Solid Earth*, 127, e2021JB022663. https://doi.org/10.1029/2021JB022663
- Li, B., Jónsson, S., S., Suhendi, C., Liu, J., Li, D., Delorme, A., Klinger, Y., & Mai, P. M. (2025). Breaching a seismic gap: the 2025 magnitude 7.7 Myanmar earthquake. *Preprint*. https://doi.org/10.21203/rs.3.rs-6734121/v1

Liu, C., Bizzarri, A., & Das, S. (2014). Progression of spontaneous in-plane shear faults from sub-Rayleigh to compressional wave rupture speeds. *Journal of Geophysical Research: Solid Earth*, 119(11), 8331–8345. https://doi.org/10.1002/2014JB011187

Madariaga, R. (1977). High-frequency radiation from crack (stress drop) models of earthquake faulting. *Geophysical Journal International*, 51(3), 625–651. https://doi.org/10.1111/j.1365-246X.1977.tb04211.x

Madariaga, R. (1979). On the relation between seismic moment and stress drop in the presence of stress and strength heterogeneity. *Journal of Geophysical Research*, 84(B5), 2243–2250. https://doi.org/10.1029/JB084iB05p02243

Madariaga, R. (1983). High frequency radiation from dynamic earthquake fault models. *Annales de Geophysique*, 1(1), 17–23.

Manighetti, I., Campillo, M., Bouley, S., & Cotton, F. (2007). Earthquake scaling, fault segmentation, and structural maturity. *Earth and Planetary Science Letters*, 253(3–4), 429–438. https://doi.org/10.1016/j.epsl.2006.11.004

Mello, M., Bhat, H. S., & Rosakis, A. J. (2016). Spatiotemporal properties of Sub-Rayleigh and supershear rupture velocity fields: Theory and experiments. *Journal of the Mechanics and Physics of Solids*, 93, 153–181. https://doi.org/10.1016/j.jmps.2016.02.031

Miller, D. D. (1998). Distributed shear, rotation, and partitioned strain along the San Andreas fault, central California. *Geology*, 26(10), 867–870. https://doi.org/10.1130/0091-7613(1998)026<0867:DSRAPS>2.3.CO;2

Mount, V. S., & Suppe, J. (1987). State of stress near the San Andreas fault: Implications for wrench tectonics. *Geology*, 15(12), 1143–1146. https://doi.org/10.1130/0091-7613(1987)15<1143:SOSNTS>2.0.CO;2

Page, M. T., Dunham, E. M., & Carlson, J. M. (2005). Distinguishing barriers and asperities in near-source ground motion. *Journal of Geophysical Research: Solid Earth*, 110, B11302, https://doi.org/10.1029/2005JB003736

Peng, Z., Lei, X., Wang, D., Si, X., Mach, P., Zhong, Q., Ding, C., Deng Y., Qin, M., & Miao, S. (2025). Mainshock rupture properties, aftershock activities and remotely triggered seismicity associated with the 2025 Mw7.7 Sagaing Fault earthquake in Myanmar. *Earthquake Research Advances*, In Press. https://doi.org/10.1016/j.eqrea.2025.100413

Robinson, D. P., Das, S., & Searle, M. P. (2010). Earthquake fault superhighways. *Tectonophysics*, 493(3–4), 236–243. https://doi.org/10.1016/j.tecto.2010.01.010

Savage, J. C. (1965). The stopping phase on seismograms. *Bulletin of the Seismological Society of America*, 55(1), 47–58. https://doi.org/10.1785/BSSA0550010047

Shi, Z., & Ben-Zion, Y. (2006). Dynamic rupture on a bimaterial interface governed by slip-weakening friction. *Geophysical Journal International*, 165(2), 469–484. https://doi.org/10.1111/j.1365-246X.2006.02853.x

Sleep, N. H., & Ma, S. (2008). Production of brief extreme ground acceleration pulses by nonlinear mechanisms in the shallow subsurface. *Geochemistry, Geophysics, Geosystems*, 9(3), Q03008. https://doi.org/10.1029/2007GC001863

Sleep, N. H. (2018). Searching for spot-fire earthquakes triggered during the 2004 Parkfield mainshock. Poster Presentation at 2018 SCEC Annual Meeting, CA.

Somerville, P. G., & Graves, R. W. (2003). Characterization of earthquake strong ground motion. *Pure and Applied Geophysics*, 160, 1811–1828. https://doi.org/10.1007/s00024-003-2407-z

Svetlizky, I., Bayart, E., & Fineberg, J. (2019). Brittle fracture theory describes the onset of frictional motion. *Annual Review of Condensed Matter Physics*, 10, 253–273. https://doi.org/10.1146/annurev-conmatphys-031218-013327

Thai Meteorological Department. (2008). Thai seismic monitoring network. *International Federation of Digital Seismograph Networks*. Retrieved from https://www.fdsn.org/networks/detail/TM/

Tun, S. T., & Watkinson, I. M. (2017). Chapter 19: The Sagaing Fault, Myanmar. In Barber, A. J., Zaw, K., & Crow, M. J. (Eds.), *Myanmar: Geology, resources and tectonics* (Vol. 48, pp. 413–441). London: Geological Society. https://doi.org/10.1144/M48.19

USGS (2025). https://earthquake.usgs.gov/earthquakes/eventpage/us7000pn9s/executive

Vera, F., Carrillo-Ponce, A., Crosetto, S., Kosari, E., Metzger, S., Motagh, M., Liang, Y., Lyu, S., Petersen, G., Saul, J., Sudhaus, H., Symmes-Lopetegui, B., Than, O., Xiao, H., & Tilmann, F. (2025). Supershear rupture along the Sagaing Fault seismic gap: The 2025 Myanmar Earthquake. *The Seismic Record*, 5(3), 289–299. https://doi.org/10.1785/0320250025

Wang, D., Mori, J., & Koketsu, K. (2016). Fast rupture propagation for large strike-slip earthquakes. *Earth and Planetary Science Letters*, 440, 115–126. https://doi.org/10.1016/j.epsl.2016.02.022

Wang, R., Schurr, B., Milkereit, C., Shao, Z., & Jin, M. (2011). An improved automatic scheme for empirical baseline correction of digital strong-motion records. *Bulletin of the Seismological Society of America*, 101(5), 2029–2044. https://doi.org/10.1785/0120110039

Wang, Y., Sieh, K., Tun, S. T., Lai, K.-Y., & Myint, T. (2014). Active tectonics and earthquake potential of the Myanmar region. *Journal of Geophysical Research: Solid Earth*, 119(4), 3767–3822. https://doi.org/10.1002/2013JB010762

- Wessel, P., Luis, J. F., Uieda, L., Scharroo, R., Wobbe, F., Smith, W. H. F., & Tian, D. (2019). The Generic Mapping Tools Version 6. *Geochemistry, Geophysics, Geosystems*, 20(11), 5556–5564. https://doi.org/10.1029/2019GC008515
- Xia, K., Rosakis, A. J., & Kanamori, H. (2004). Laboratory earthquakes: The sub-Rayleigh-to-supershear rupture transition. *Science*, 303(5665), 1859–1861. https://doi.org/10.1126/science.1094022
- Xiong, X., Shan, B., Zhou, Y. M., Wei, S. J., Li, Y. D., Wang, R. J., & Zheng, Y. (2017). Coulomb stress transfer and accumulation on the Sagaing Fault, Myanmar, over the past 110 years and its implications for seismic hazard. *Geophysical Research Letters*, 44(10), 4781–4789. https://doi.org/10.1002/2017GL072770
- Xu, S., Ben-Zion, Y., Ampuero, J.-P., & Lyakhovsky, V. (2015). Dynamic ruptures on a frictional interface with off-fault brittle damage: Feedback mechanisms and effects on slip and near-fault motion. *Pure and Applied Geophysics*, 172(5), 1243–1267. https://doi.org/10.1007/s00024-014-0923-7
- Xu, S., & Ben-Zion, Y. (2017). Theoretical constraints on dynamic pulverization of fault zone rocks. *Geophysical Journal International*, 209(1), 282–296. https://doi.org/10.1093/gji/ggx033
- Xu, S., Fukuyama, E., Yamashita, F., Mizoguchi, K., Takizawa, S., & Kawakata, H. (2018). Strain rate effect on fault slip and rupture evolution: Insight from meter-scale rock friction experiments. *Tectonophysics*, 733, 209–231. https://doi.org/10.1016/j.tecto.2017.11.039
- Xu, S., Fukuyama, E., & Yamashita, F. (2019). Robust estimation of rupture properties at propagating front of laboratory earthquakes. *Journal of Geophysical Research: Solid Earth*, 124(1), 766–787. https://doi.org/10.1029/2018JB016797
- Xu, S., Fukuyama, E., Yamashita, F., Kawakata, H., Mizoguchi, K., & Takizawa, S. (2023). Fault strength and rupture process controlled by fault surface topography. *Nature Geoscience*, 16(1), 94–100. https://doi.org/10.1038/s41561-022-01093-z
- Yao, Q. (2017). Dynamic modeling of earthquake sources on rough faults (Doctoral dissertation). San Diego: University of California, San Diego & San Diego State University.
- Yao, S., & Yang, H. (2025). Rupture phases reveal geometry-related rupture propagation in a natural earthquake. *Science Advances*, 11(4), eadq0154. https://doi.org/10.1126/sciadv.adq0154
- Ye, L., Lay, T., & Kanamori, H. (2025). The 28 March 2025 $M_{\rm w}$ 7.8 Myanmar Earthquake: Preliminary analysis of an ~480 km long intermittent supershear rupture. *The Seismic Record*, 5(3), 260–269. https://doi.org/10.1785/0320250021

Supporting Information for

Intermittent supershear rupture punctuated by barrier-induced stopping phase during the 2025 $M_{\rm w}$ 7.8 Myanmar Earthquake: Evidence from near-fault strong motion observation

Xiaotian Ding¹, Shiqing Xu^{1,*}, Lingling Ye¹

¹Department of Earth and Space Sciences, Southern University of Science and Technology, Shenzhen, China

*Corresponding author: xusq3@sustech.edu.cn

Contents of this file

Text S1 to S9 Figures S1 to S17 Tables S1 to S2

Introduction

In this supporting information, we show the basic idea for understanding the relation between the 2.5D and 3D models (Text S1), explain the model setup for conducting numerical simulations (Text S2 to S7), present the methods for evaluating waveform fit (Text S8), and briefly summarize the contents of related figures and tables (Text S9). Several additional figures (Figures S1 to S17) and tables (Tables S1 to S2) are also included, to provide further support for the ideas and/or statements presented in the main text.

Text S1. The relation between the 2.5D and 3D models

Figure S1 shows the equivalent mapping between a 2.5D model and a conventional 3D model. The 2.5D model is similar to a conventional 2D model, featured by a 1D fault embedded in a 2D plane (the XY plane, see Fig. S1a), but can also take into account the stress communication at the vertical boundary (in Z direction) of the seismogenic zone (Weng & Ampuero, 2019, 2020). From a 3D point of view, the 2.5D model can be considered as a 2D fault plane embedded in a 3D full space, where the finite seismogenic zone width ($W_{2.5D}$) can lead to a rupture transition from crack-like to pulse-like, once the along-strike rupture propagation distance exceeds some threshold value proportional to $W_{2.5D}$ (Day, 1982). Since a buried earthquake on a vertical strike-slip fault (as the full-space case in Fig. S1a) can be approximated by the superposition of a surface-breaking earthquake on a similar fault (as the half-space case in Fig. S1b) and its "mirror" above the free surface (Pollard & Segall, 1987; Luo et al., 2017), it follows that there is an equivalent mapping between the seismogenic zone width in the 2.5D full-space model ($W_{2.5D}$) and that in the 3D half-space model (W_{3D}):

$$W_{2.5D} = 2 \cdot W_{3D} \tag{S1}$$

According to the kinematic source model of Ye et al. (2025) for subfault F3 (Fig. 1b) and the above mapping relation (Eq. S1), we choose W_{3D} as 7.5 km for the 3D model and $W_{2.5D}$ as 15 km for the 2.5D model.

In this study, structured meshes are implemented in both the 2.5D and 3D models, as the spectral element method (SEM) is chosen to solve the dynamic rupture problem. The number of Gauss-Lobatto-Legendre (NGLL) points per element is set to 5. The element size is set as 250 m for the 2.5D model and 500 m for the 3D model, equivalent to a grid resolution of \sim 62.5 m and \sim 125 m, respectively. The Courant–Friedrichs–Lewy (CFL) number is set to 0.50 for the 2.5D model and 0.13 for the 3D model, resulting in timesteps of 0.0039 s and 0.00125 s, respectively. The 2.5D model domain extends 250 km in the strike direction (X \in [-100 km, 150 km]) and 150 km in the fault-normal direction (Y \in [-75 km, 75 km]). The 3D model extends the same 250 km in the strike direction (X \in [-40 km, 40 km]), and 40 km in the depth direction (Z \in [-40 km, 0]). For convenience, later we use non-negative values for discussing depth in the 3D model (as in Fig. S2). Absorbing

boundary conditions are applied to all surrounding boundaries, except for the free surface in the 3D model (Fig. S1b), which is treated with a traction-free boundary condition.

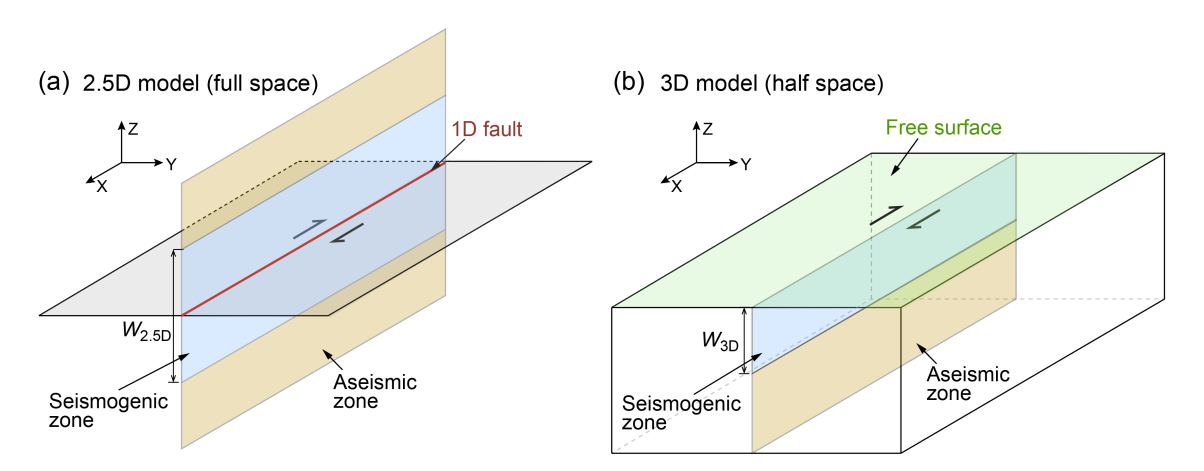


Figure S1. Schematic illustration of the relation between (a) a 2.5D model in full space and (b) a 3D model in half space. For (a) and (b), a vertical strike-slip fault is considered, with blue area and yellow area representing the seismogenic zone and aseismic zone, respectively, and $W_{2.5D}$ and W_{3D} indicating the corresponding seismogenic zone width. In (a), red line indicates a 1D fault embedded in a 2D plane (in gray). In (b), the free surface is colored in green.

Text S2. Elastic properties

Proper setup of elastic properties in numerical simulations is crucial for comparing simulated waveforms with data. Here, we estimate the related values based on the regional velocity structure for Myanmar (Shiddiqi et al., 2019). After some averaging over the seismogenic depth, P wave speed (C_P) and S wave speed (C_S) are set as 5580 m/s and 3310 m/s, respectively. Subsequently, Rayleigh wave speed (C_R) is estimated as 3031 m/s following Aki and Richards (2002), and mass density (ρ) is empirically determined as 2633 kg/m³ following Brocher (2005). For simplicity, we don't consider any spatial variations of elastic properties in the current simulations, such as a material contrast across the Sagaing fault, a sedimentary basin in the top few kilometers, or a fault damage zone with reduced wave speeds (Peng et al., 2025). These complexities are left for the future work aiming to simulate more realistic ground motions.

Text S3. Friction laws

As in Ding et al. (2023), a time-weakening friction (TWF) law is used to artificially nucleate the rupture on the modeled subfault F3, by forcing friction coefficient f to drop with time t at a constant rate of $(f_s - f_d) \cdot V_r^{\text{TWF}}/L_0$:

$$f = \min\left\{\max\left\{f_0 - \frac{(f_s - f_d) \cdot (v_r^{\text{TWF}} \cdot t - r)}{L_0}, f_d\right\}, f_s\right\}$$
 (S2)

where f_0 is the initial shear-to-normal stress ratio $(\sigma_{xy}^i/|\sigma_{yy}^i|)$, to be introduced in Text S4), f_s and f_d are the static and dynamic friction coefficient, respectively, V_r^{TWF} is a constant speed at which rupture is forced to propagate, r is the distance from the nucleation site on subfault F3.

After a certain amount of propagation distance, a slip-weakening friction (SWF) law will take over the control, with friction coefficient f linearly decreasing with slip δ until reaching a critical value D_c :

$$f = \begin{cases} f_{\rm s} - (f_{\rm s} - f_{\rm d}) \cdot \frac{\delta}{D_{\rm c}}, & \text{if } \delta \le D_{\rm c} \\ f_{\rm d}, & \text{if } \delta > D_{\rm c} \end{cases}$$
 (S3)

where f_s and f_d retain the same meanings and values as those in TWF. Accordingly, static and dynamic strength can be defined as $\tau_s = f_s \cdot |\sigma_n|$ and $\tau_d = f_d \cdot |\sigma_n|$, respectively, with $|\sigma_n|$ being the magnitude of normal stress (see Text S4, S5 and S7). Under the control of SWF, rupture can propagate spontaneously with a varying rupture speed. In most cases, we use the above strategy involving both TWF and SWF to simulate a variety of rupture speeds approaching the target NPW station on subfault F3. In some other cases, we employ TWF only but with different constant speeds (with respect to $\sqrt{2}C_s$) to explore the corresponding wavefield under a (quasi)steady-state supershear rupture.

Text S4. Basic setup of the initial stress field

The fundamental part of the initial stress field, in the absence of any further model complexities, is set based on the previous modeling works on strike-slip earthquakes (Dunham & Archuleta, 2004; Ding et al., 2023) as well as trial-and-error specifically made for the 2025 Myanmar earthquake. Without losing generality, initial normal stress (σ_{yy}^i) is set at -50 MPa (negative for compression) and strike-parallel initial shear stress (σ_{yz}^i) is set at 24 MPa in the 2.5D model. In the 3D model, dip-parallel initial shear stress (σ_{yz}^i) is chosen as 0 MPa at all depths, while σ_{yy}^i and

 σ_{xy}^{i} are assumed to linearly taper toward zero over the uppermost 1 km (Fig. S2a), to ensure a close similarity with the 2.5D model over much of the seismogenic zone and a compatibility with the free surface condition as assumed in previous studies (Ma, 2008; Kaneko & Lapusta, 2010).

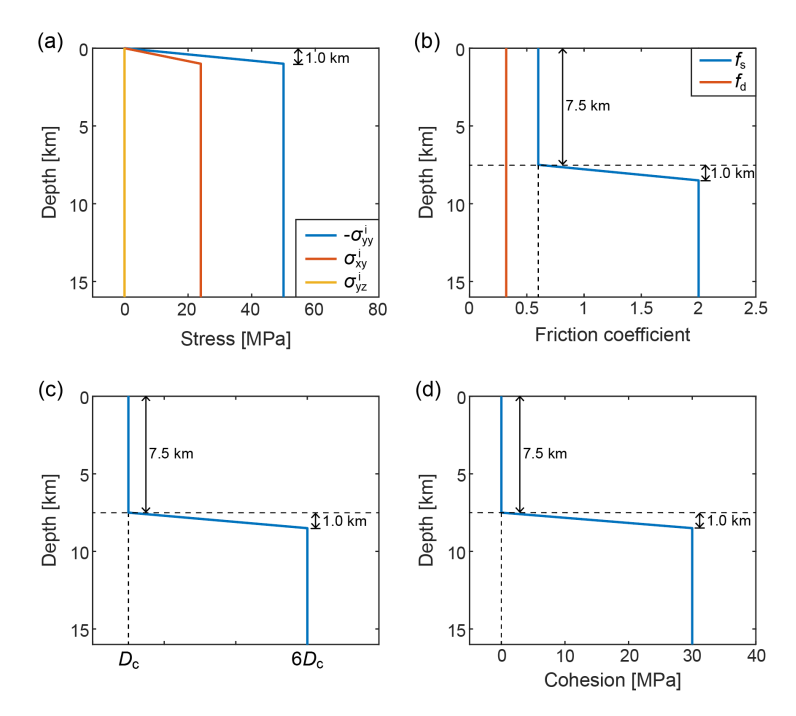


Figure S2. Additional setup for the 3D model. (a) Along-depth distribution of various stress components. (b) Along-depth distribution of static and dynamic friction coefficient. (c) Along-depth distribution of slip-weakening distance, expressed by the basic unit of D_c used in the 2.5D model. (d) Along-depth distribution of fault cohesion. Except for the stress field in the uppermost 1 km, all the parameters above the depth of 7.5 km share the same values as in the 2.5D model. For (a)-(d), positive depth corresponds to the negative direction along the Z-axis (see Fig. S1).

Text S5. Setup of the seismogenic zone

While the seismogenic zone can be directly defined via the parameter $W_{2.5D}$ in the 2.5D model (Fig. S1a), it needs to be manually set in the 3D model. Here for the 3D model, the down-dip transition from the seismogenic zone to the aseismic zone (Fig. S1b) is realized by assigning increased-then-saturated values of static friction coefficient (f_s) (Fig. S2b), slip-weakening distance ($D_c \rightarrow 6D_c$) (Fig. S2c) and fault cohesion (the intrinsic part of fault strength that is independent of normal stress) below the depth of 7.5 km (Fig. S2d). The assumed values have been tested to be strong enough to restrict the simulated 3D ruptures in the top 7.5 km or so.

Text S6. Additional setup for promoting/arresting rupture toward the south/north

In order to simulate dynamic ruptures with different speeds, we follow the method of Dunham and Archuleta (2004) to introduce an asperity to the south of rupture nucleation site on subfault F3 (different from the actual hypocenter on subfault F1). The asperity is realized by increasing initial (strike-parallel) shear stress τ_i from 24 MPa toward a constant higher level of τ_i^{Asp} , with a purpose to promote rupture acceleration including possible supershear transition toward the south. The exact value of τ_i^{Asp} varies from case to case, and will be tuned to control the rupture speed and the slip pulse amplitude approaching the target NPW station. On the opposite side, static friction coefficient f_s is assumed to rise from 0.6 toward 5.0, in order to impede rupture propagation toward the north (not the focus of current study). It should be noted that the above methods for promoting or arresting rupture propagation are arbitrary. The main purpose is to output a southward-propagating rupture, whose wavefield can be checked with the observation at the NPW station, rather than to reproduce precisely the inverted rupture process on subfault F3 (Ye et al., 2025).

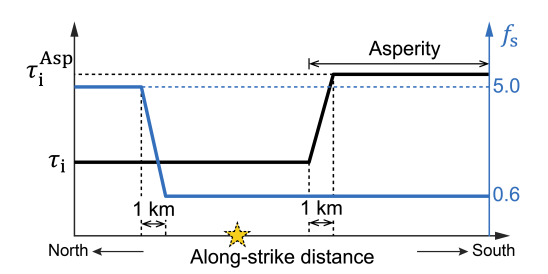


Figure S3. Additional setup of initial shear stress τ_i and static friction coefficient f_s . τ_i (in black) is assumed to increase and then saturate at a higher level τ_i^{Asp} toward the south, in order to promote rupture propagation in this direction. f_s (in blue) is assumed to exhibit a similar behavior but toward the north, in order to arrest rupture in this direction. The region with increased τ_i is referred to as an asperity. Yellow pentagram indicates rupture nucleation site on the modeled subfault F3, which is set arbitrarily and should not be mixed with the actual observation.

Text S7. Realization of a barrier near the NPW station

We try three different ways to model a barrier near the NPW station: a fault patch with (a) spatially decreased initial shear stress (τ_i) (Fig. S4a), (b) spatially increased magnitude of initial normal

stress ($|\sigma_n| = |\sigma_{yy}^i|$) (Fig. S4b), and (c) spatially increased static friction coefficient (f_s) (Fig. S4c). For all the three, the related quantity first deviates from its original level by a constant gradient, but later remains at a new, constant level after a certain along-strike distance. We use the related gradient of initial shear stress $\nabla \tau_i$ or that of static strength $\nabla \tau_s = \nabla (f_s \cdot |\sigma_n|)$ to assess the effect of barrier strength. In addition, we also examine the effect of barrier location, defined by the relative distance of its starting position to the NPW station ($X_{Bar-NPW}$). $X_{Bar-NPW}$ is positive and negative when the barrier is located on the southern and northern side of the NPW station, respectively.

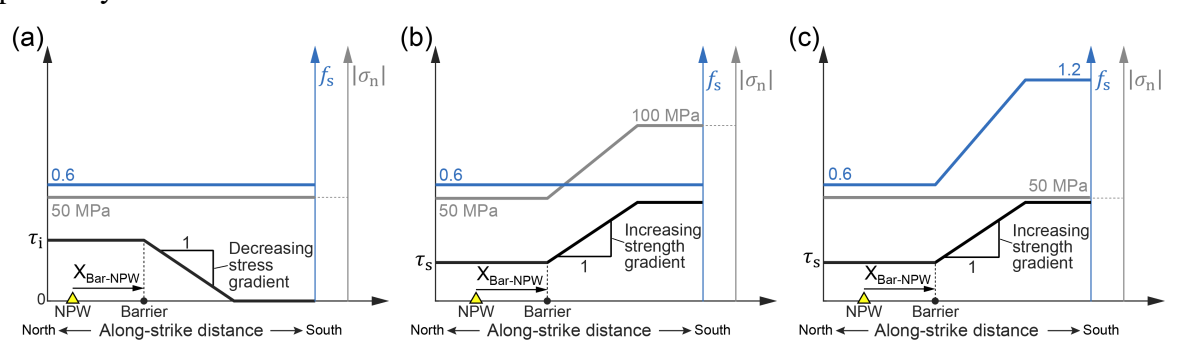


Figure S4. Realization of a fault barrier near the NPW station, associated with (a) spatially decreased initial shear stress τ_i , (b) spatially increased initial normal stress $|\sigma_n|$, and (c) spatially increased static friction coefficient f_s . Decreasing stress gradient and increasing strength gradient are evaluated by $\nabla \tau_i$ and $\nabla \tau_s = \nabla (f_s \cdot |\sigma_n|)$, respectively. $X_{Bar-NPW}$ defines the starting position of the barrier relative to the NPW station, with positive/negative indicating the barrier on the southern/northern side of the NPW station.

Text S8. Methods for evaluating waveform fit

A metric in terms of root-mean-square-error (RMSE) is introduced to evaluate the similarity between the simulated synthetic waveform and the observed one. A lower RMSE value indicates a higher similarity between the two and hence a better waveform fit. The core steps for evaluating waveform fit via RMSE are summarized below, following and modifying the methods in Xu et al. (2019):

Step 1: Resample the synthetic waveform under the 2.5D or 3D model from its original timestep (see Text S1) to a new one of 0.01 s, in order to match the sampling rate of the observation (100 Hz) (Lai et al., 2025).

Step 2: Cut the observed waveform in a shorter time window and the synthetic one in a longer time window. Then pick a starting point of the longer synthetic waveform.

Step 3: Use the observed waveform as a template to slide against the synthetic one, and compute the related RMSE (Eq. S4) over the time window of Stage-I to III (see Fig. 1c; we purposely ignore Stage-IV since our current simulations cannot reproduce the enduring oscillations behind the main pulse; however, we include Stage-I since this part is crucial for baseline alignment of the velocity waveform):

$$RMSE = \sqrt{\frac{\sum_{i=1}^{2 \text{ or } 3}^{3} \sum_{j=1}^{N_{t}} (v_{ij}^{\text{syn}} - v_{ij}^{\text{ obs}})^{2}}{(2 \text{ or } 3) \cdot N_{t}}}$$
 (S4)

where $V_{ij}^{\rm syn}$ is the extracted part of synthetic waveform, $V_{ij}^{\rm obs}$ is the observed waveform, and N_t is the total number of samples during Stage-I to III. The index i denotes the waveform component, corresponding to FP and FN for the 2.5D model, and FP, FN, and UD for the 3D model. Similarly, a sub-RMSE for each component, taking FP as an example (i = 1), can be computed:

RMSE_FP =
$$\sqrt{\frac{\sum_{j=1}^{N_t} (v_{1j}^{\text{syn}} - v_{1j}^{\text{obs}})^2}{N_t}}$$
 (S5)

where $V_{1j}^{\rm syn}$ and $V_{1j}^{\rm obs}$ represent the corresponding FP component of the synthetic and observed waveforms, respectively. After the above operation, store the computed values of RMSE and sub-RMSE.

Step 4: Shift the starting point of the longer synthetic waveform by one timestep (0.01 s) and repeat Step 3, until reaching the end of synthetic waveform.

Step 5: Evaluate the distribution of RMSE as a function of shifted number of timestep. The one with a minimal value of RMSE (Fig. S5a) will be used to show the corresponding waveform fit for each component, and the associated values of RMSE FP and RMSE FN (Fig. S5b).

Later, when constructing the phase diagram such as in Fig. 3d, we repeat the above steps for each combination of model parameters, and plot the obtained value of RMSE (from Step 5) in the parameter space. After exploring a range of model parameters, we choose the preferred cases as

those "interior points" (i.e., not at the boundary) with lower (not necessarily the lowest) values of RMSE.

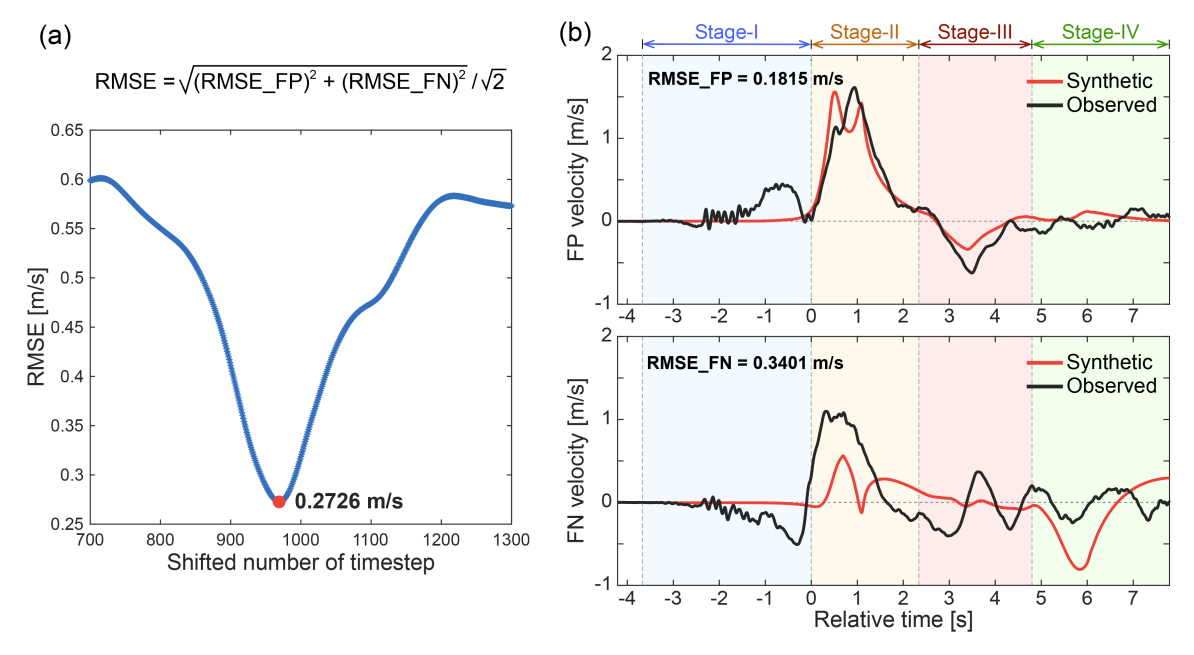


Figure S5. (a) Distribution of root-mean-square-error (RMSE) as a function of shifted number of timestep. RMSE, defined in Eq. (S4), is a metric for evaluating the general similarity between synthetic and observed waveforms over all components (here over the FP and FN components). (b) The corresponding waveforms when RMSE (evaluated over Stage-I to III) reaches a minimum (the red dot in panel (a)). RMSE_FP (Eq. S5) and RMSE_FN indicates a sub version of RMSE for the FP and FN component, respectively.

Text S9. Summary

Figures S6–S17 show additional simulation results to support various statements made in the main text (Figs. S6–S14 under the 2.5D model, and Figs. S15–S17 under the 3D model): waveform fits under a simulated subshear rupture (Fig. S6), a simulated incipient supershear rupture (Fig. S7) and six simulated (quasi)steady-state supershear ruptures (Fig. S8), comparison between on-fault slip velocity and off-fault particle velocity (Fig. S9), effect of barrier location on waveform fit (Figs. S10 and S11), effect of barrier strength on waveform fit (Fig. S12), preferred cases with barrier realized by increased normal stress and the related phase diagrams (Fig. S13), preferred cases with barrier realized by increased static friction coefficient and the related phase diagrams (Fig. S14), and selected preferred cases under the 3D model (Figs. S15–S17).

Table S1 summarizes the basic parameters and their values, common for both the 2.5D and 3D models (excluding those for the aseismic zone in the 3D model). Table S2 lists the specific parameter values used in some simulation cases, without or with a fault barrier.

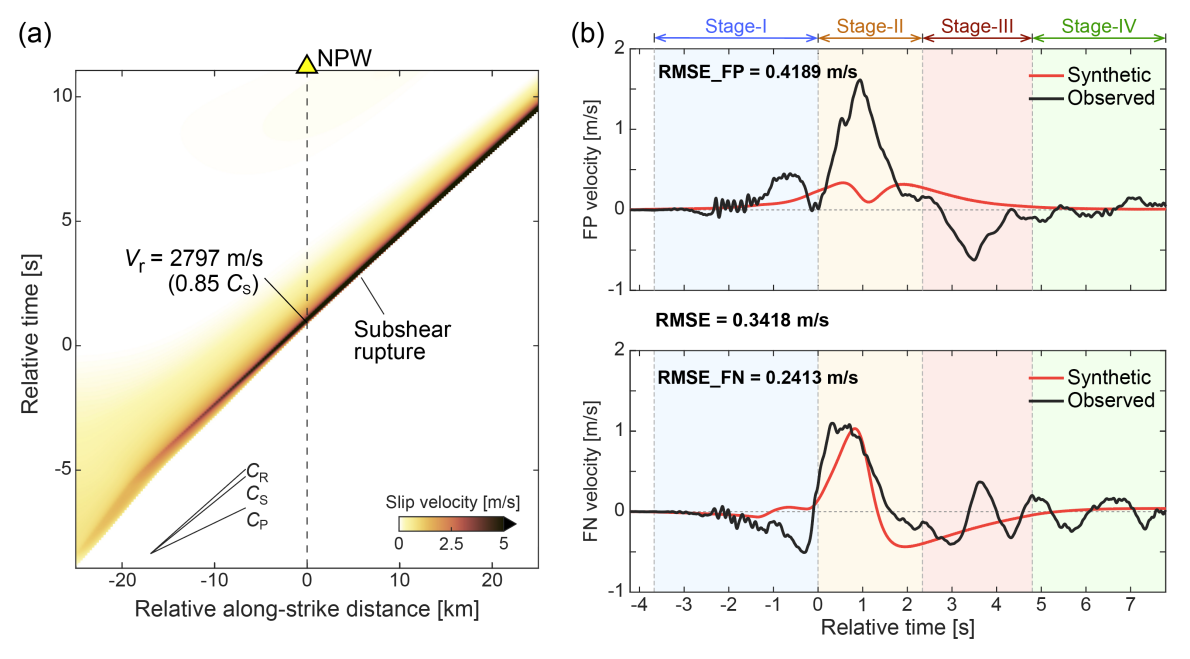


Figure S6. (a) Evolution of slip velocity for a simulated subshear rupture under the 2.5D model. (b) The related waveform fit with data at the NPW station. See Text S8 and Fig. S5 for the meanings and computations of RMSE, RMSE_FP and RMSE_FN.

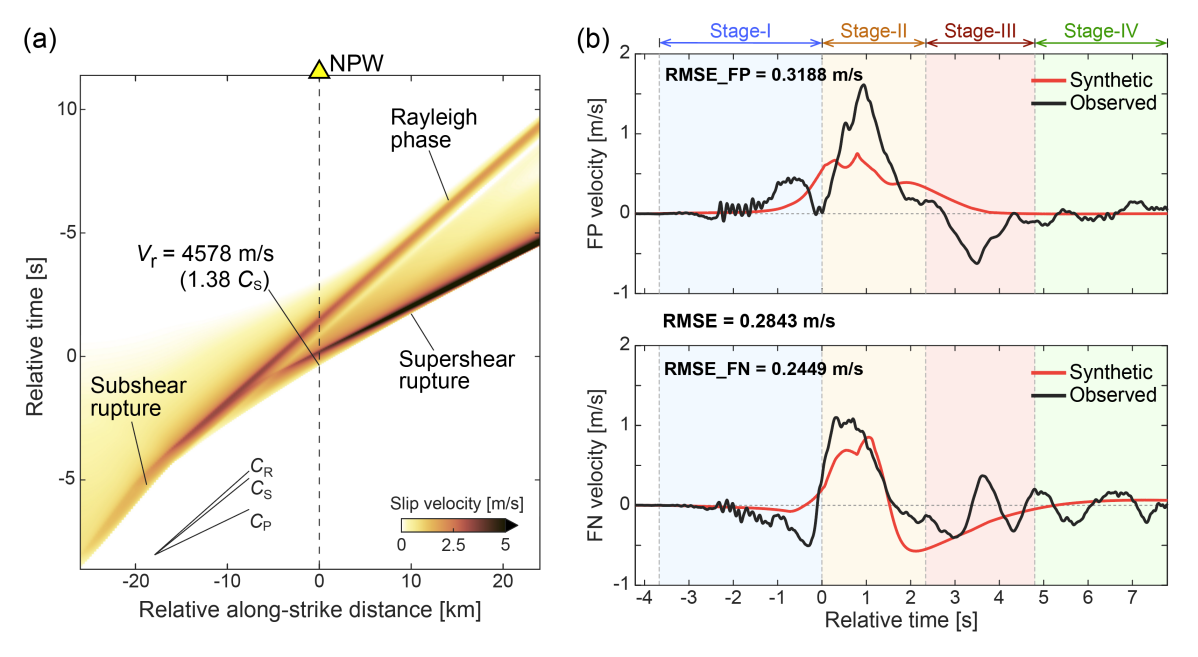


Figure S7. Similar to Figure S6, but for an incipient supershear rupture that has just transitioned from subshear near the NPW station.

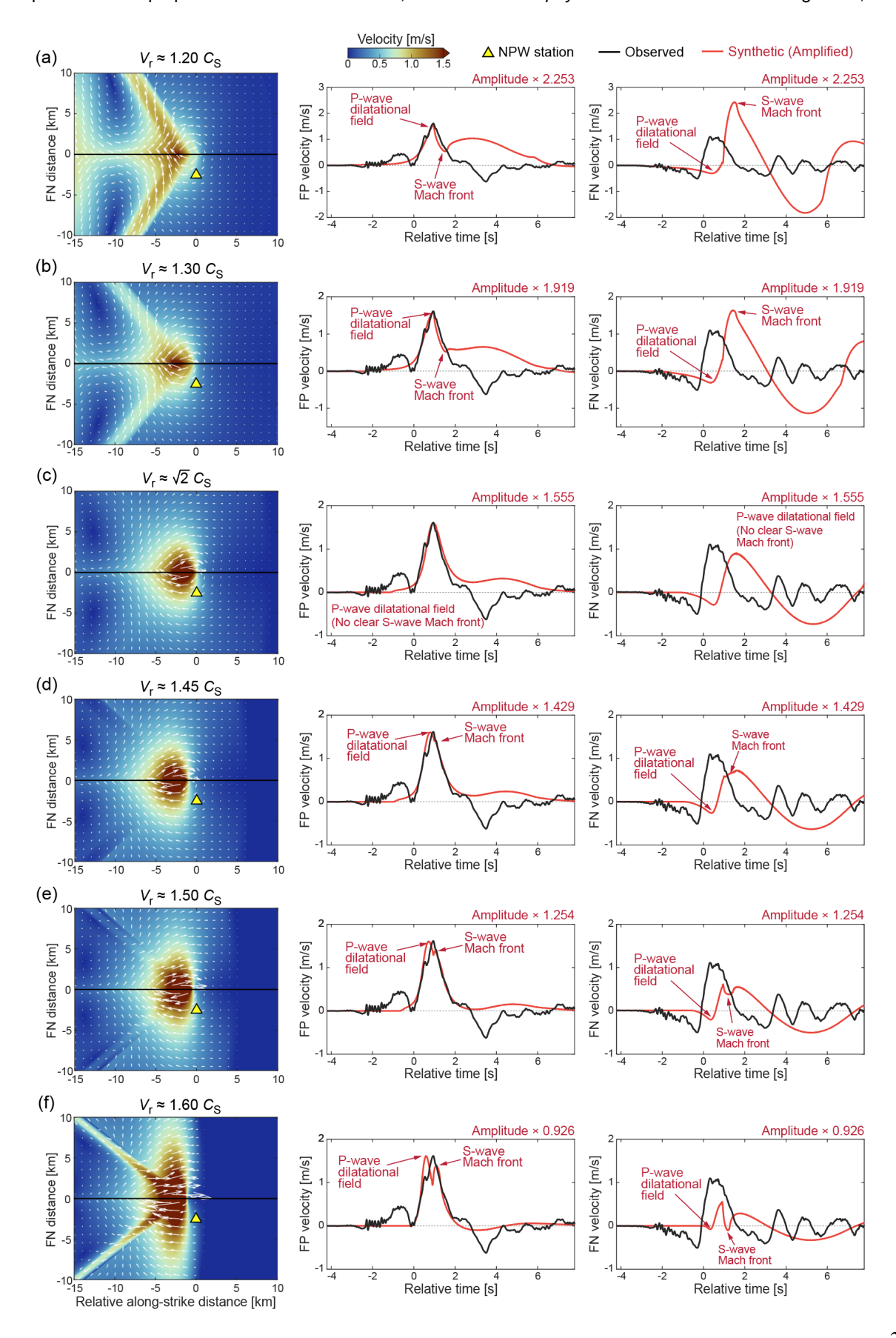


Figure S8. (a)-(f) Simulated wavefields for six (quasi)steady-state supershear ruptures under the control of time-weakening friction (TWF) in the 2.5D model (first column), and the related waveform comparison with the observation at the NPW station (second and third columns). In the first column, rupture propagates to the "right" (south), with background color showing the magnitude of particle velocity and white arrows indicating the direction and relative magnitude of particle motion. Positive FP in the second column and positive FN in the third column correspond to the "left" and "up" in the first column, respectively.

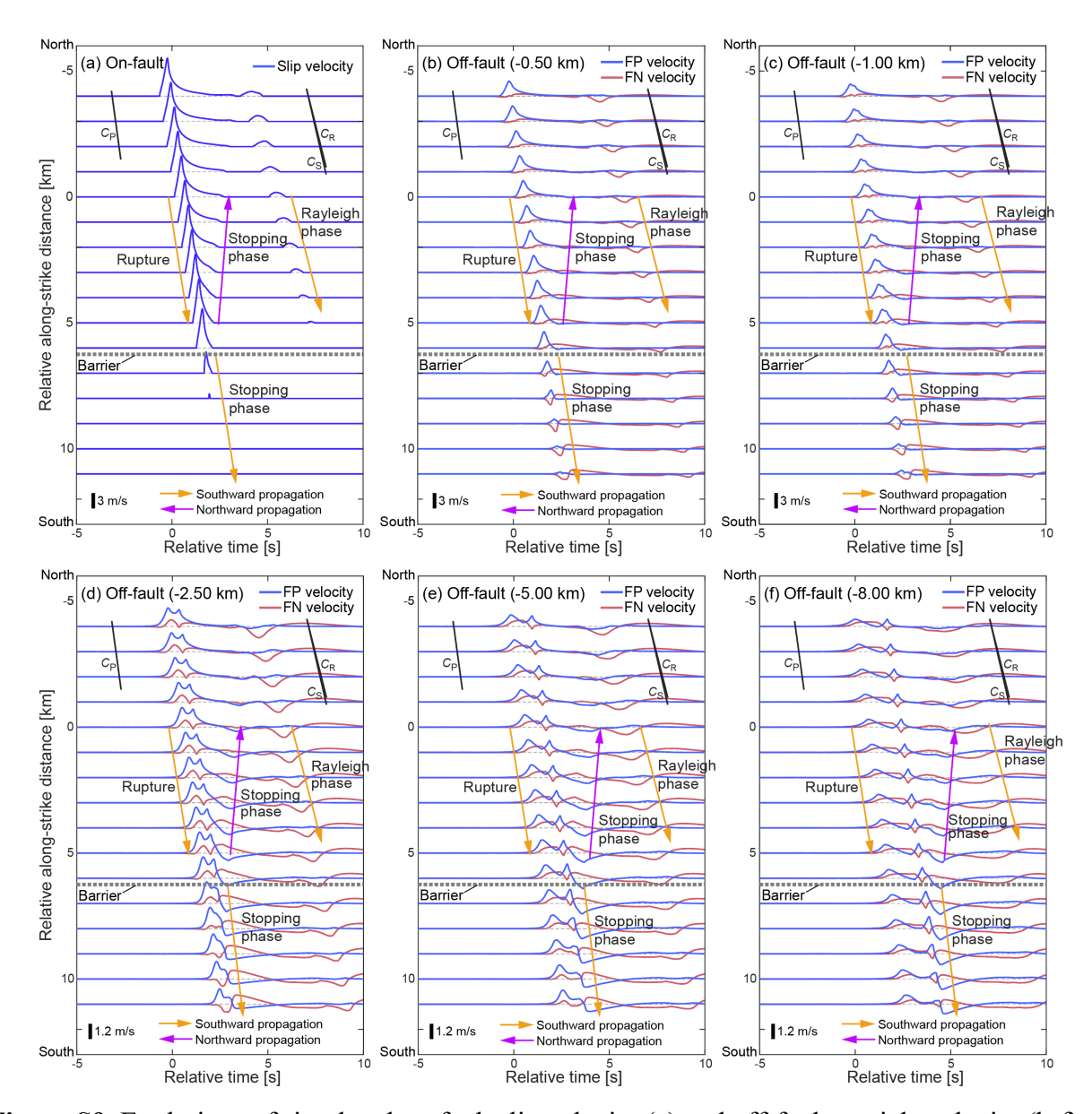


Figure S9. Evolutions of simulated on-fault slip velocity (a) and off-fault particle velocity (b-f) at a series of along-strike distances or off-fault distances. The results here correspond to the case shown in Figs. 3a and 3b.

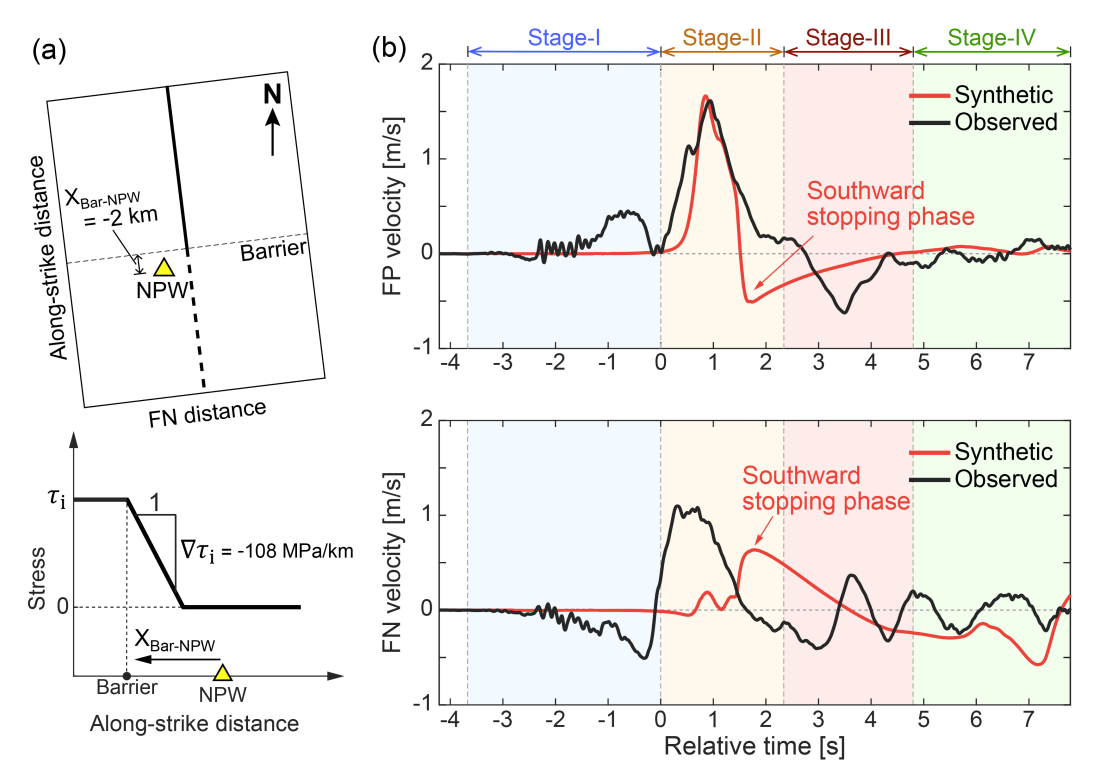


Figure S10. Similar to Figs. 3a and 3b, but with a barrier located on the northern side of the NPW station ($X_{Bar-NPW} = -2 \text{ km}$, instead of the previous value of 6.25 km). For this case, the simulated negative FP pulse (in red) reflects the southward-propagating part of the stopping phase (for reference, see the simulated wavefield in Fig. 3a or the waveforms in Fig. S9).

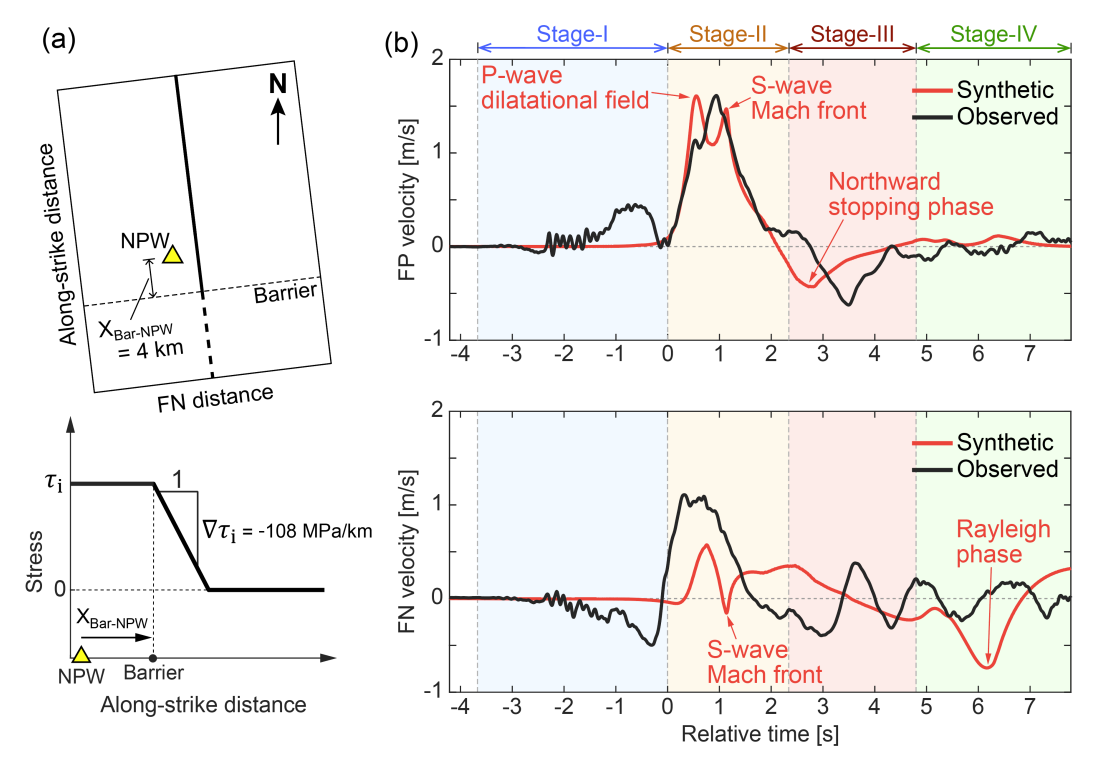


Figure S11. Similar to Figs. 3a and 3b, but with a barrier located closer to the NPW station on its southern side ($X_{Bar-NPW} = 4$ km, instead of the previous value of 6.25 km). For this case, the simulated negative FP pulse (in red) arrives earlier than the observed one (in black).

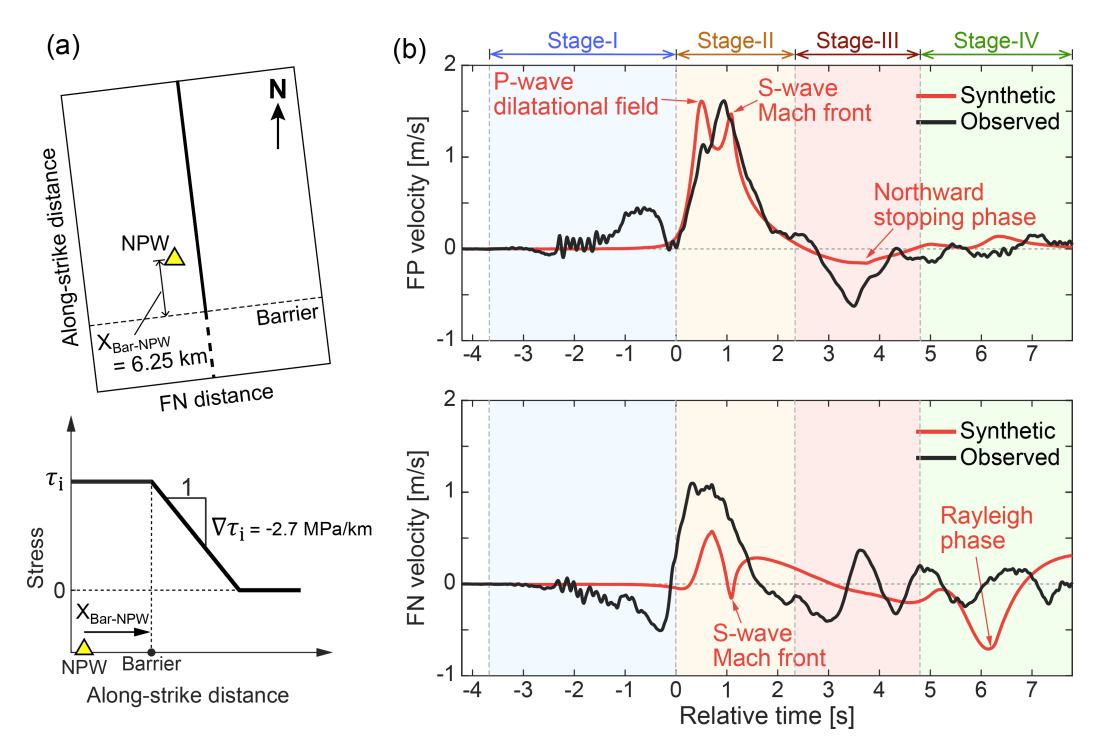


Figure S12. Similar to Figs. 3a and 3b, but with a weaker barrier ($\nabla \tau_i = -2.7$ MPa/km, instead of the previous value of -108 MPa/km). For this case, the amplitude of the simulated negative FP pulse (in red) is much reduced.

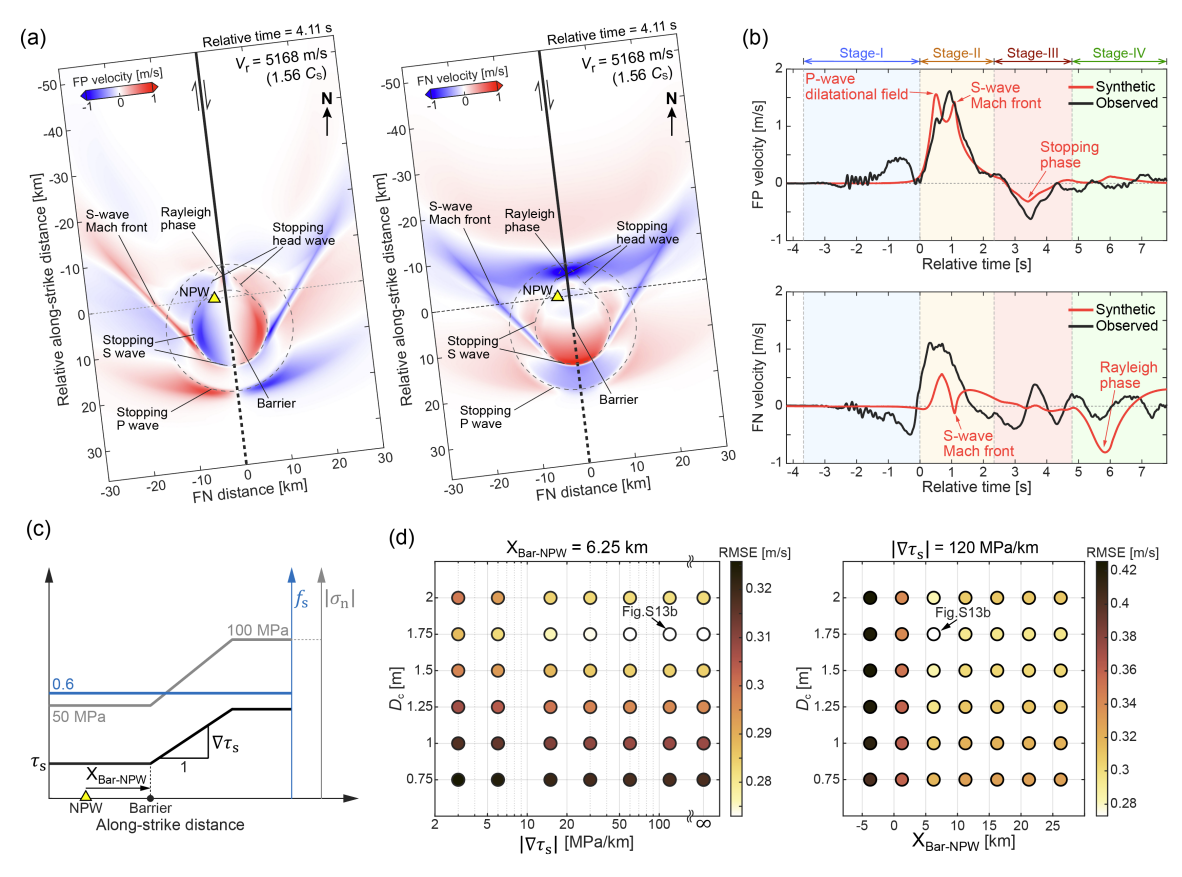


Figure S13. Similar to Fig. 3, but with the barrier realized by a spatial increase of initial normal stress $|\sigma_n|$ and hence static strength $\tau_s = f_s \cdot |\sigma_n|$. Here $\nabla \tau_s$ represents increasing strength gradient (Text S7, Fig. S4b).

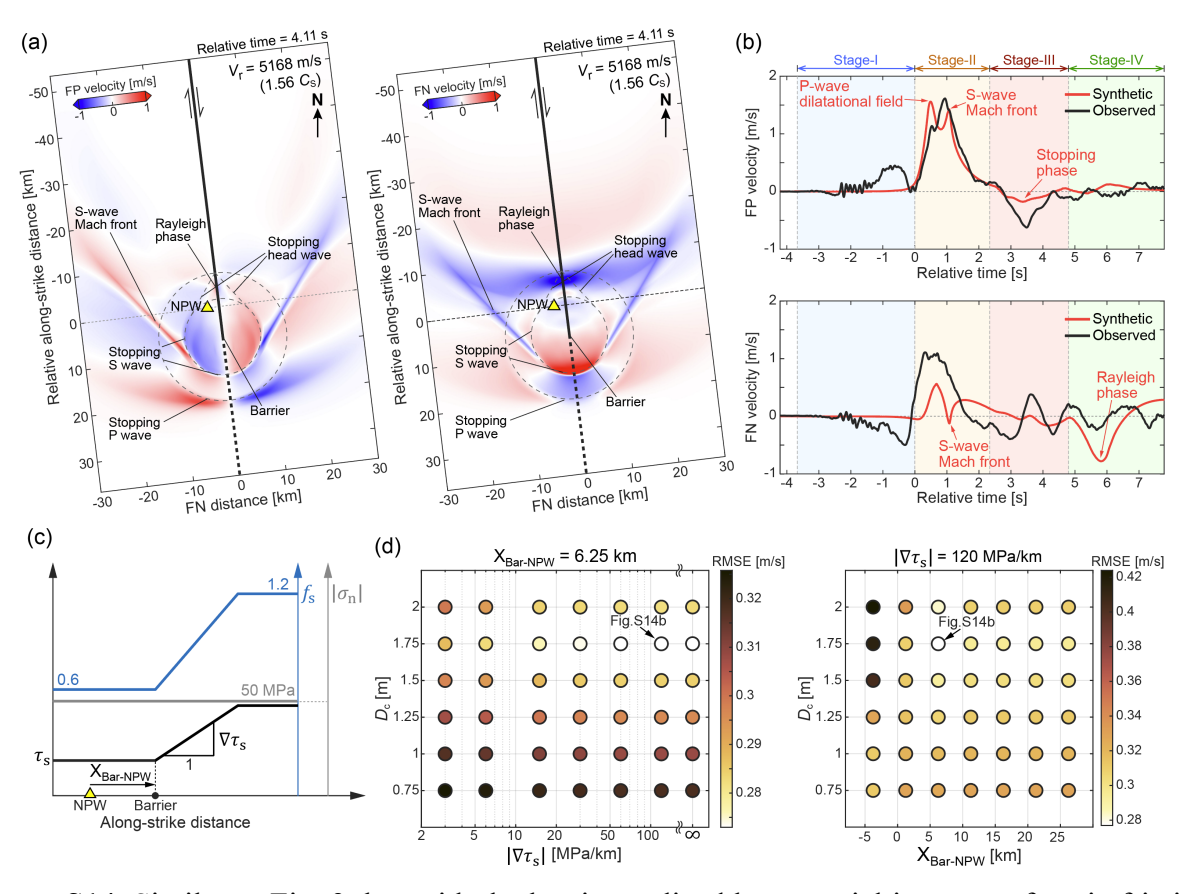


Figure S14. Similar to Fig. 3, but with the barrier realized by a spatial increase of static friction coefficient f_s and hence static strength $\tau_s = f_s \cdot |\sigma_n|$. Here $\nabla \tau_s$ represents increasing strength gradient (Text S7, Fig. S4c).

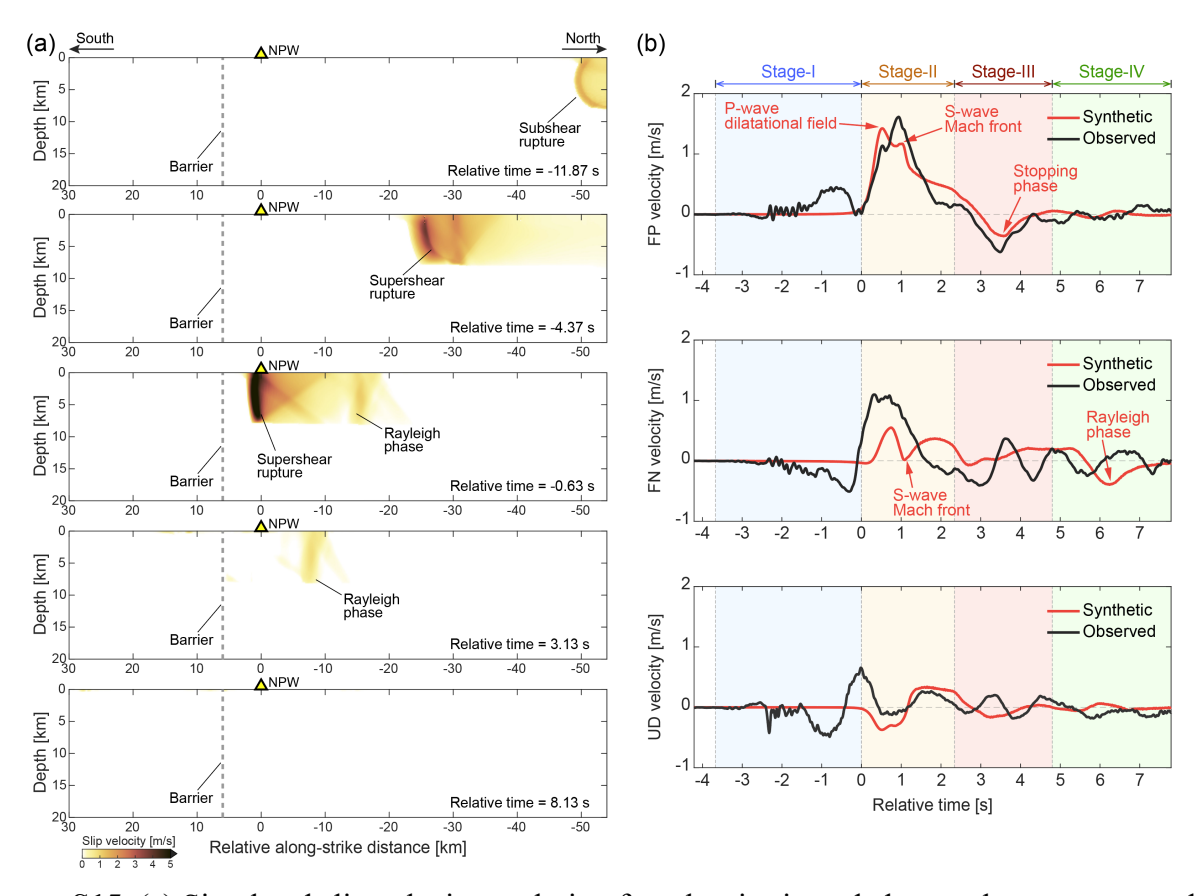


Figure S15. (a) Simulated slip velocity evolution for a barrier-impeded supershear rupture under the 3D model. (b) The related waveform fit with data at the NPW station. For this case, the barrier is realized by a spatial decrease of initial shear stress (see Table S2 for more information).

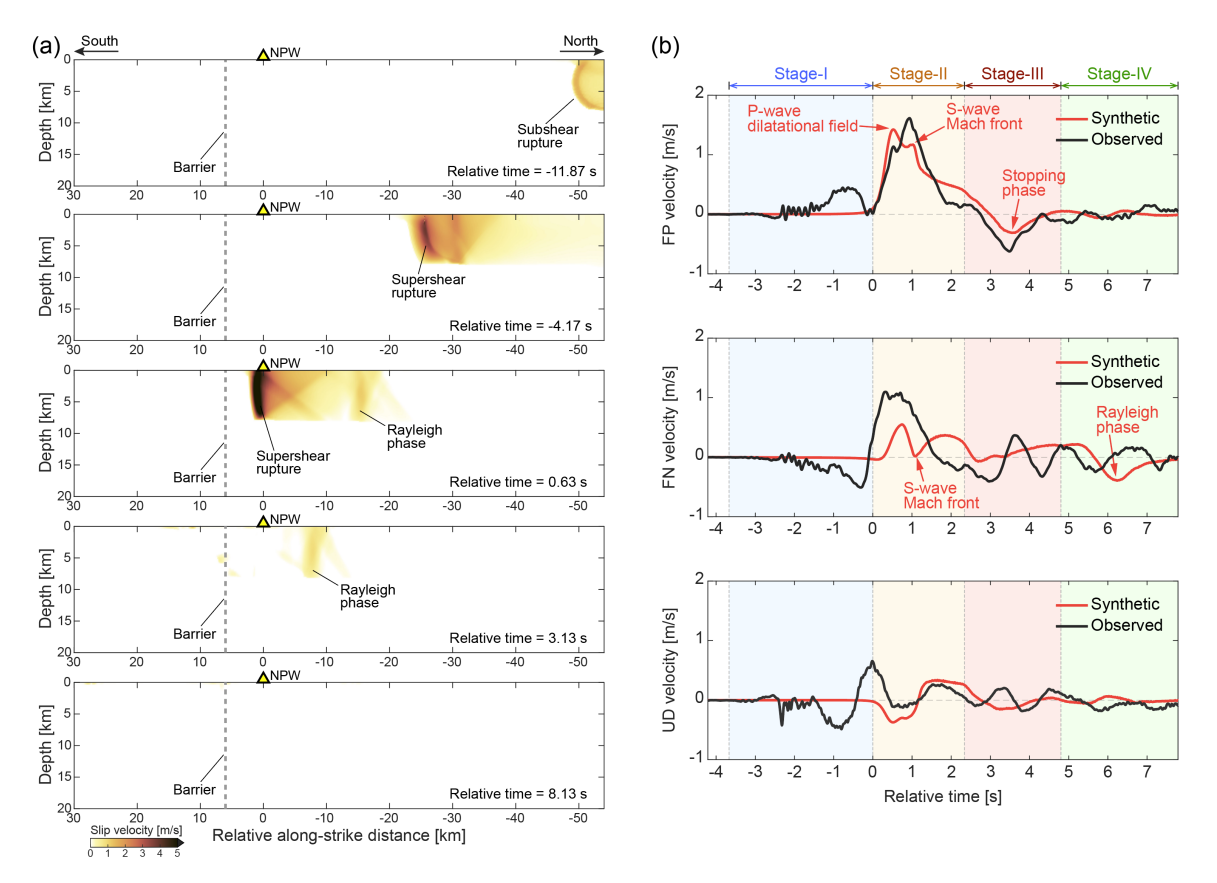


Figure S16. Similar to Fig. S15, but with the barrier realized by a spatial increase of initial normal stress (see Table S2 for more information).

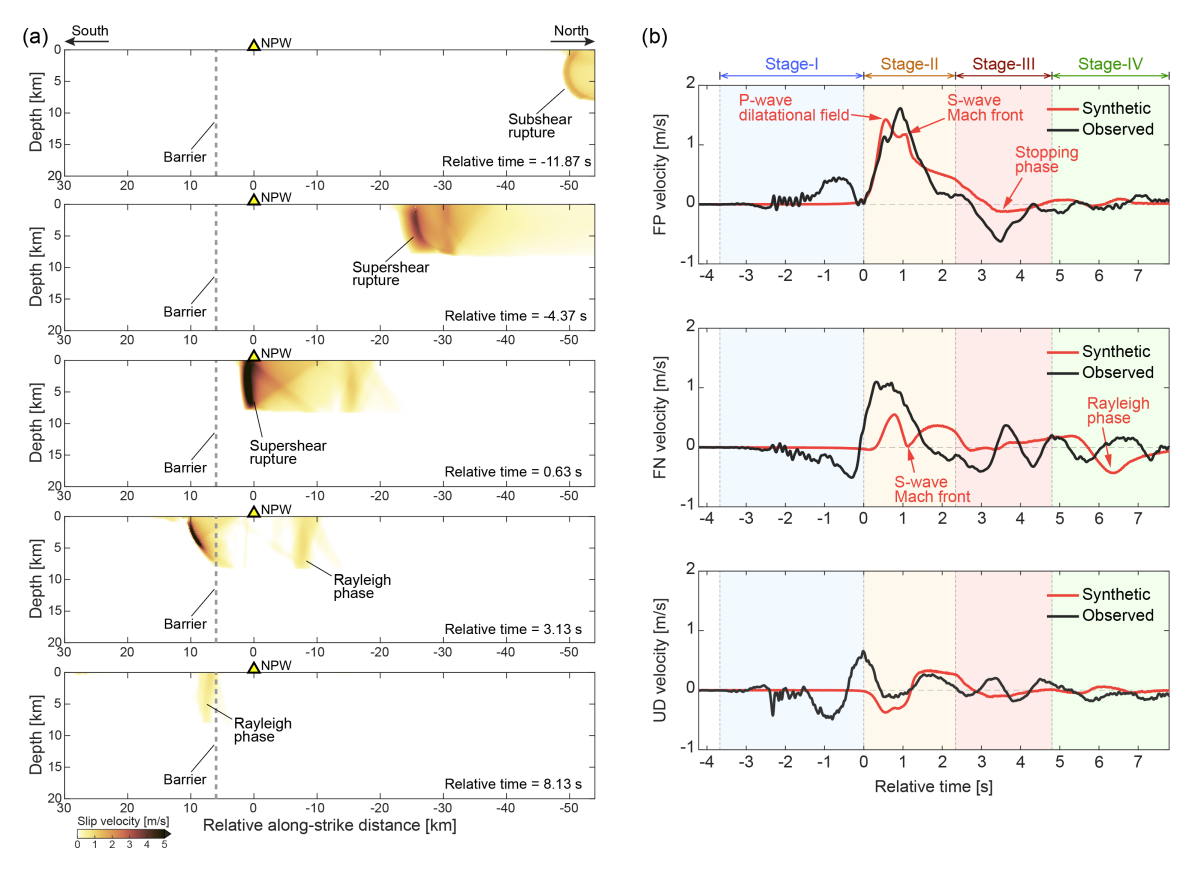


Figure S17. Similar to Fig. S15, but with the barrier realized by a spatial increase of static friction coefficient (see Table S2 for more information).

 Table S1. Basic parameters and their values

Parameters	Values
P wave speed (C_P)	5580 m/s
S wave speed (C_S)	3310 m/s
Rayleigh wave speed (C_R)	3031 m/s
Mass density (ρ)	2633 kg/m^3
Static friction coefficient (TWF & SWF) (f_s)	0.60
Dynamic friction coefficient (TWF & SWF) (f_d)	0.32
Rupture propagation speed (TWF, most cases) (V_r^{TWF})	2000 m/s
Characteristic length (TWF) (L_0)	2 km
Slip-weakening distance (SWF) (D_c)	(0.75 - 2.00) m
Initial normal stress ($\sigma_{\rm n} = \sigma_{\rm yy}^{\rm i}$)	-50 MPa
Initial strike-parallel shear stress (non-asperity) ($ au_i = \sigma_{xy}^i$)	24 MPa
Initial dip-parallel shear stress (σ_{yz}^{i})	0 MPa
Initial strike-parallel shear stress (asperity) ($\tau_i = \tau_i^{Asp}$)	(24.50 — 27.00) MPa

Table S2. Certain parameters and their values used in specific cases

Figure #	Parameters	Values
Figs. 2a and 2b	Slip-weakening distance (<i>D</i> _c)	0.75 m
	Initial strike-parallel shear stress (asperity) (τ_i^{Asp})	25.75 MPa
Figs. 2c and 2d	Slip-weakening distance (D_c) Initial strike-parallel shear stress (asperity) (τ_i^{Asp})	1.75 m 27.00 MPa
Figs. 3a, 3b, 4, S5, S9, S10, and S11	Slip-weakening distance (D_c) Initial strike-parallel shear stress (asperity) (τ_i^{Asp}) Magnitude of decreasing stress gradient ($ \nabla \tau_i $)	1.75 m 27.00 MPa 108 MPa/km
Fig. S6	Slip-weakening distance (D_c) Initial strike-parallel shear stress (asperity) (τ_i^{Asp})	1.25 m 24.50 MPa
Fig. S7	Slip-weakening distance (D_c) Initial strike-parallel shear stress (asperity) (τ_i^{Asp})	1.25 m 26.00 MPa
Fig. S12	Slip-weakening distance (D_c) Initial strike-parallel shear stress (asperity) (τ_i^{Asp}) Magnitude of decreasing stress gradient $(\nabla \tau_i)$	1.75 m 27.00 MPa 2.7 MPa/km
Figs. S13 and S14	Slip-weakening distance (D_c) Initial strike-parallel shear stress (asperity) (τ_i^{Asp}) Magnitude of increasing strength gradient $(\nabla \tau_s)$	1.75 m 27.00 MPa 120 MPa/km
Fig. S15	Slip-weakening distance (D_c) Initial strike-parallel shear stress (asperity) (τ_i^{Asp}) Magnitude of decreasing stress gradient $(\nabla \tau_i)$	1.25 m 27.00 MPa 54 MPa/km
Figs. S16 and S17	Slip-weakening distance (D_c) Initial strike-parallel shear stress (asperity) (τ_i^{Asp}) Magnitude of increasing strength gradient ($ \nabla \tau_s $)	1.25 m 27.00 MPa 60 MPa/km

References From the Supporting Information

Aki, K., & Richards, P. G. (2002). *Quantitative seismology* (2nd Ed.). Mill Valley, CA: University Science Books.

Brocher, T. M. (2005). Empirical relations between elastic wavespeeds and density in the earth's crust. *Bulletin of the Seismological Society of America*, 95(6), 2081–2092. https://doi.org/10.1785/0120050077

Day, S. (1982). Three-dimensional finite difference simulation of fault dynamics: Rectangular faults with fixed rupture velocity. *Bulletin of the Seismological Society of America*, 72(3), 705–727. https://doi.org/10.1785/BSSA0720030705

Kaneko, Y., & Lapusta, N. (2010). Supershear transition due to a free surface in 3-D simulations of spontaneous dynamic rupture on vertical strike-slip faults. *Tectonophysics*, 493(3–4), 272–284. https://doi.org/10.1016/j.tecto.2010.06.015

Luo, Y., Ampuero, J.-P., Miyakoshi, K., & Irikura, K. (2017). Surface rupture effects on earthquake moment-area scaling relations. *Pure and Applied Geophysics*, 174, 3331–3342. https://doi.org/10.1007/s00024-017-1467-4

Ma, S. (2008). A physical model for widespread near-surface and fault zone damage induced by earthquakes. *Geochemistry*, *Geophysics*, *Geosystems*, 9(11), Q11009, https://doi.org/10.1029/2008GC002231

Pollard, D. D., & Segall, P. (1987). Theoretical displacements and stresses near fractures in rock: With applications to faults, joints, veins, dikes, and solution surfaces. In Atkinson, B. K. (Ed.), *Fracture mechanics of rock* (Chap. 8, pp. 277–349). London: Academic Press. https://doi.org/10.1016/b978-0-12-066266-1.50013-2

Shiddiqi, H. A., Tun, P. P., & Ottemöller, L. (2019). Minimum 1D velocity model and local magnitude scale for Myanmar. *Seismological Research Letters*, 90(5), 1923–1936. https://doi.org/10.1785/0220190065

Weng, H., & Ampuero, J.-P. (2019). The dynamics of elongated earthquake ruptures. *Journal of Geophysical Research: Solid Earth*, 124(8), 8584–8610. https://doi.org/10.1029/2019JB017684

Weng, H., & Ampuero, J.-P. (2020). Continuum of earthquake rupture speeds enabled by oblique slip. *Nature Geoscience*, 13(12), 817–821. https://doi.org/10.1038/s41561-020-00654-4